Doctoral Dissertation

博士論文

# Development of a Morphological Indicator of Microalgal Cu$^{2+}$ Removal Efficiency

（微細藻類の Cu$^{2+}$除去効率の形態インジケーターの開発）

A Dissertation Submitted for the Degree of Doctor of Philosophy
August 2021

令和 3 年 8 月博士（理学）申請
Department of Chemistry, Graduate School of Science,
The University of Tokyo

東京大学大学院理学系研究科化学専攻

XU, Muzhen

徐 木貞

# Development of a Morphological Indicator of Microalgal Cu$^{2+}$ Removal Efficiency

by

## XU, Muzhen

Submitted to the Department of Chemistry
in partial fulfillment of the requirements for the degree of
Doctor of Philosophy
at
The University of Tokyo

# Abstract

Heavy metal removal from wastewater is one of the most concerned worldwide environmental problems because heavy metals are stable and hazardous elements, which are non-biodegradable and could be bio-accumulated. To effectively eradicate toxic heavy metals from wastewater and stabilize the ecosystem, various methods have been reported, which fall into two categories: conventional physico-chemical methods and bioremediation methods. Among them, microalgae-based bioremediation methods have attracted much attention in the past few decades for treating wastewater polluted with heavy metal because of the increasing demands of more environment friendly, cost-effective, and sustainable treatment methods. However, the heavy metal removal efficiency of microalgae is far from practical use. A small amount of research has investigated the improvement of heavy metal removal efficiency of microalgae, such as immobilization, pretreatment, and genetic modification of microalgal cells. But these methods either have limited enhancement of the heavy metal removal efficiency of microalgae or potentially pose threat to the environment and human health by deploying genetically modified species.

To address these problems, directed evolution is expected to be effective for developing microalgae with much higher heavy metal removal efficiency without the problem of using new strains in wastewater treatment. However, experimental demonstration of this method is challenging because there is no non-invasive or label-free indicator to identify the highly efficient cells. The presently available indicators, like the ion intensity of heavy metals within each cell and the fluorescence intensity of metal fluorescent probes, are invasive or require labelling.

In this doctoral work, I proposed and experimentally demonstrated an intelligent cellular morphological indicator for identifying the heavy metal removal efficiency of *Euglena gracilis* in a non-invasive and label-free manner. Specifically, I recognized a morphological meta-feature of *E. gracilis* cells under 7.5 μM $Cu^{2+}$ exposure by analysing single-cell images via machine learning algorithms, and demonstrated a strong monotonic correlation (Spearman's $\rho = -0.82$, $P = 2.1 \times 10^{-5}$) between this morphological meta-feature and the $Cu^{2+}$ removal efficiency of nineteen *E. gracilis* clones. Our findings firmly

suggest that the morphology of *E. gracilis* cells can serve as an effective heavy metal removal efficiency indicator. The intelligent morphological indicator has great potential, when combined with the recently developed powerful sorting methods such as the high-throughput image-activated cell sorter, for directed-evolution-based development of *E. gracilis* with extremely high heavy metal removal efficiency for practical wastewater treatment worldwide.

Thesis Supervisor: Keisuke Goda

Title: Professor of Chemistry

# Acknowledgement

My research work in this thesis has been conducted under the instructions and guidance of Prof. Keisuke Goda from September 2018 to September 2021 at the Department of Chemistry, Graduate school of Science, the University of Tokyo.

Undoubtedly, I express my great gratitude to my supervisor-Prof. Goda. Three years ago, I was admitted as a member of Goda Lab, and from that time, he continuously gave me assistance and support both of my research and life. As an academic elite, whose directions and guidance did benefit me, he provides an excellent model to our young researchers.

I am greatly thankful to my diligent team leader-Prof. Akihiro Isozaki for his constructive advice and comments about my research, our discussions about my work were very fruitful, and it is under his assistance and support that my research could go smoothly. As my leader, he tried to make better experimental conditions and readily help me when I was in trouble. Moreover, He encouraged me to apply for research grants. I therefore prepared application documents in English, and he translated them into Japanese, which is not easy, but we finally made it. Doubtlessly, Isozaki sensei's help and support would be always highly appreciated and unforgettable.

I would like to thank Prof. Kotaro Hiramatsu, Prof. Cheng Lei, and Prof. Sheng Yan, for their practical suggestions for my research. I would like to thank Dr. Dan Yuan, Jeffrey Harmon, Yuqi Zhou, Mun Hong Loo, Yuta Nakagawa, and Tsubasa Kobayashi for assisting my research and school life. I also acknowledge all other Goda Lab members for their assistance in many aspects.

I want to thank my collaborators. First, I appreciate Prof. Tomohisa Hasunuma and Prof. Yuichi Kato in Kobe University, for their assistance with my research, especially for providing me the knowledge and experimental resources of gene mutagenesis and microalgal metabolism. Also, I want to thank Yumiko Ishii in the IMSUT FACS Core Laboratory for her technical assistance with the cell preparation.

I am grateful to my family for their solid support, encouragement, and care. I would like to thank my parents and parents-in-law for their selfless support for my study abroad both spiritually and financially. I want to thank my husband Linlin Li for his

encouragement and support all the time during my Ph.D. study. It is his understanding and accompanies that help me to face and overcome all the difficulties in my study.

# Contents

# List of figures

# List of tables

# Chapter 1

# Introduction

## 1.1 Heavy metal pollution in wastewater

Water is regarded as one of the most precious resources to support the growth and proliferation of all creatures on earth. It is also crucial for human activities, as evident from their heavy industrial, domestic, and agricultural use. Most of the used water is charged as wastewater, which could contain various pollutants such as organic toxins, surfactants, mineral salts, and heavy metals (HMs). Due to water pollution, people are facing serious problems of the water crisis. Especially, HM pollution in wastewater, which mainly comes from the increasing industrial activities like mine draining and electroplating, greatly threatens the health of human beings (Figure 1-1). Because of the intrinsic properties of HMs, including high solubility in the aquatic environment, bioaccumulation, and nonbiodegradability, they can be easily absorbed by living organisms and finally accumulate in the human body along the food chain. Once the concentration of accumulated HMs exceeds the permitted one, these HMs can cause serious health disorders. For example, the largest heavy metal pollution of ground water happened in Bangladesh, with millions of inhabitants exposed to arsenic (As) and under the threat of skin lesions and cancers [1]. Some significant HMs that show toxicity to living beings includes iron (Fe), lead (Pb), zinc (Zn), cadmium (Cd), copper (Cu), mercury (Hg), chromium (Cr), As, nickel (Ni), and manganese (Mn). The permitted HM concentration in drinking water prescribed by various organizations and the corresponding health issues caused by these HMs are listed in Table 1-1.
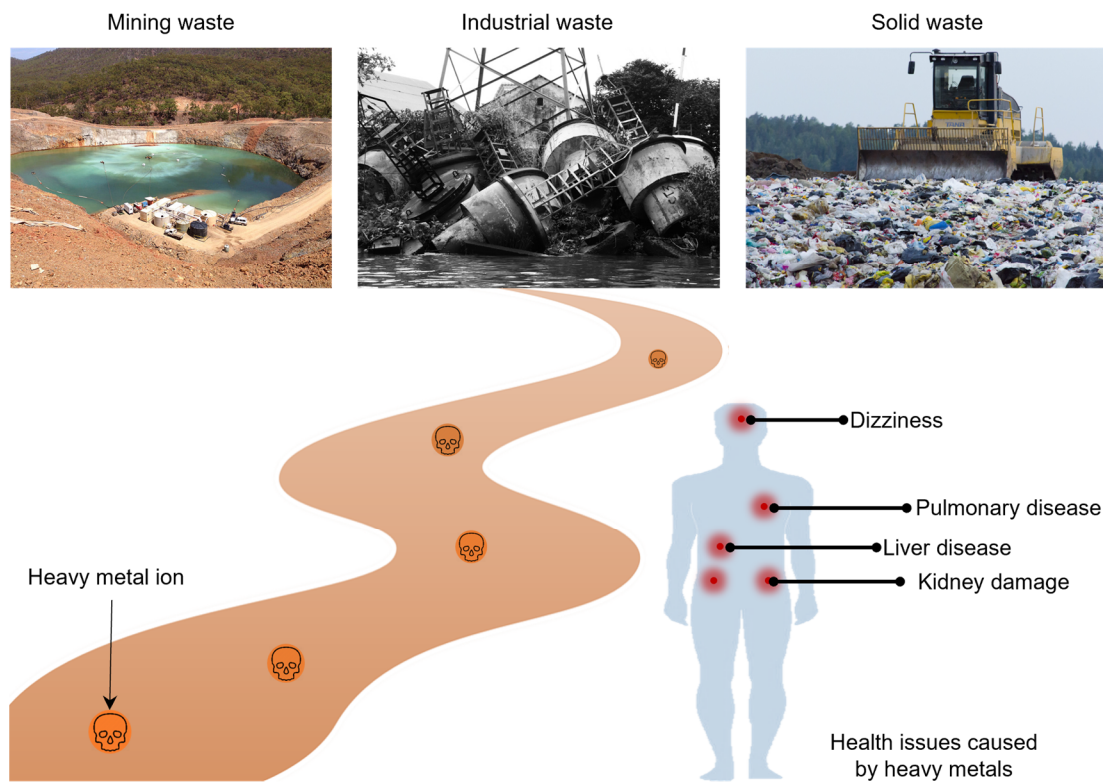
Figure 1-1. HM pollution in wastewater that originates from industrial activities and some of its harmful effects on human health. Reproduced from the Commonwealth Scientific and Industrial Research Organisation and licensed under the Creative Commons Attribution 3.0 Unported license (https://creativecommons.org/licenses/by/3.0/). Reproduced with permission from PxHere.

Table 1-1. Drinking water standards and effects on human health of some significant HMs.

| HMs | Drinking water standards | | Effects on human health | References |
|---|---|---|---|---|
| | WHO[a], 2017 (µg/L) | USEPA[b], 2018 (µg/L) | | |
| Fe | - | 300 | Alzheimer type II astrocytosis, Parkinsonism, cognitive dysfunction, and ataxia | [2] |
| Pb | 10 | 15 | Hemolytic anemia, effects on neurotransmitter levels, and organ damage | [3] |
| Zn | - | 5000 | Accumulation in muscle, liver, and gills | [4] |
| Cd | 3 | 5 | Chronic kidney disease | [5] |
| Cu | 2000 | 1300 | Alzheimer type II astrocytosis, Parkinsonism, cognitive dysfunction, and ataxia. | [2] |
| Hg | 6 | 2 | Damage to DNA and accumulation in muscle, liver, and gills | [4, 6] |
| Cr | 50 | 100 | Cancer | [7] |
| As | 10 | 10 | Cutaneous manifestations, peripheral vascular disease, gastrointestinal disturbances, alteration in the coporphyrin/ uroporphyrin excretion ratio, and cancer | [8] |
| Ni | 70 | - | Cancer of the lungs, throat, stomach, nose, and sinuses | [9] |
| Mn | - | 50 | Alzheimer type II astrocytosis, Parkinsonism, cognitive dysfunction, liver diseases, ataxia, and effects on central nervous functions | [2, 10] |

[a], World Health Organization; [b], United Stated Environmental Protection Agency

To effectively eradicate toxic HMs from wastewater and stabilize the ecosystem, various methods have been reported, which fall into two categories: conventional physico-chemical methods [11] and bioremediation methods [12, 13] (Figure 1-2). Examples of conventional physico-chemical methods are chemical precipitation [14], ion exchange [15, 16], membrane filtration [17-19], floatation [20, 21], coagulation-

flocculation [22, 23], and electrochemical methods [24, 25]. These methods are advantageous for their rapid process, ease of operation, and flexibility to different treatment conditions. However, these advantages are outweighed by the drawbacks like high operation and maintenance costs, high energy consumption, and secondary pollution due to toxic sludge formation. During the past few decades, bioremediation methods using plants [26, 27], peat moss [28], bacteria [29, 30], fungi [31, 32], and algae [33, 34] for HM removal have also received much attention on account of their sustainability, environmental-friendliness, and cost-efficiency. These methods are growing, active, and have great potential as an alternative to conventional physico-chemical methods.
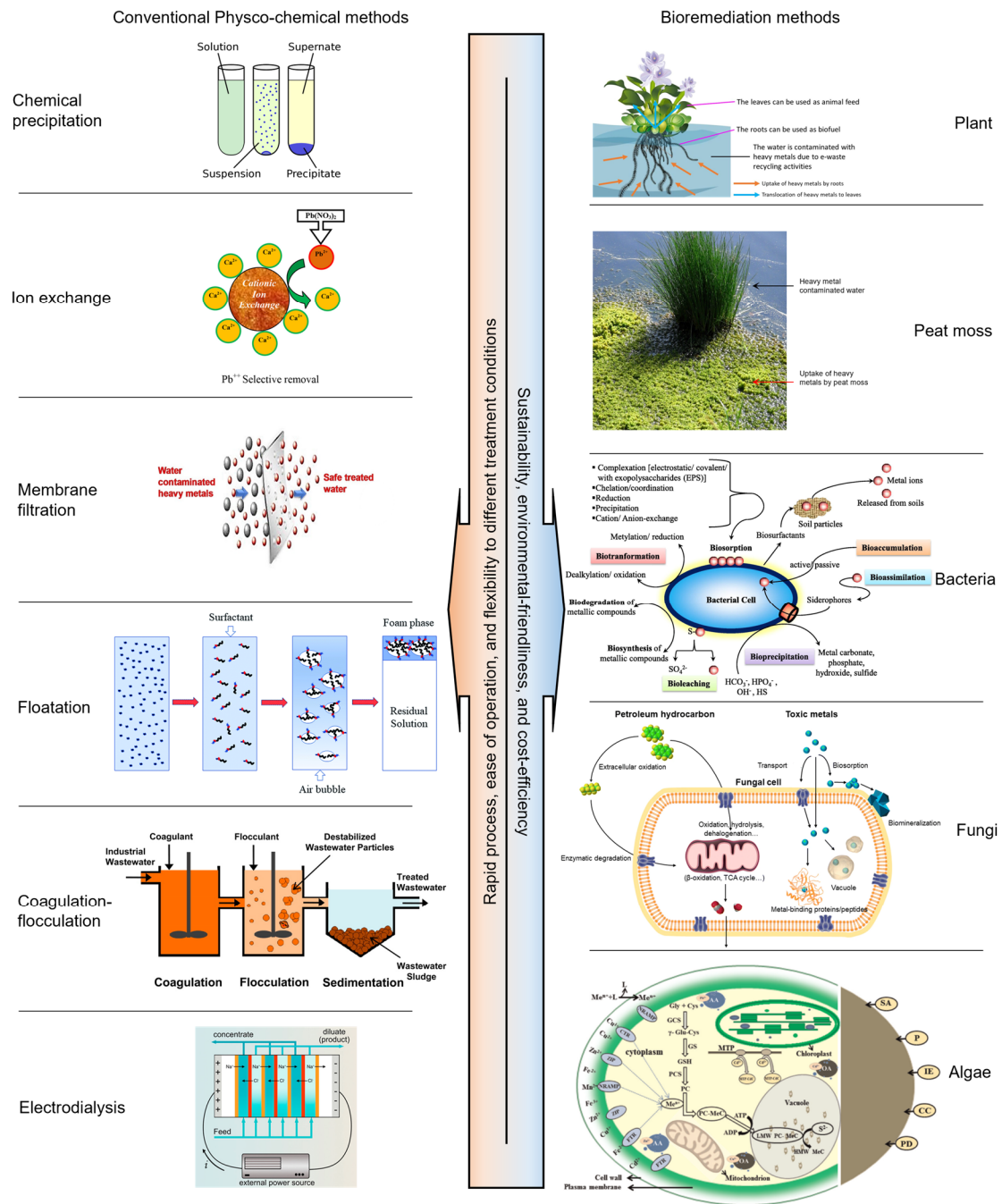
Figure 1-2. Schematic of conventional physico-chemical methods and bioremediation methods. Reproduced with permission from Stockio.com. Reproduced with permission from ref [16]. Copyright 2018 Elsevier. Reproduced with permission from ref [19]. Copyright 2019 Elsevier. Reproduced from ref [21] with permission from the Royal Society of Chemistry. Reproduced with permission from ref [23]. Copyright 2016 American Chemical Society. Reproduced with permission from ref [25]. Copyright 2016 Elsevier. Reproduced with permission from ref [27]. Copyright 2020 Elsevier. Reproduced with permission from Pixabay with minor modifications. Reproduced with the permission from ref [30]. Copyright 2019 Elsevier. Reproduced with permission from ref [32]. Copyright 2020

## 1.2 Bioremediation methods

Nowadays, bioremediation methods have attracted great academic and industrial interest because they are low-cost, eco-friendly, and able to remove HMs at low concentrations compared with conventional physico-chemical methods. Bioremediation methods used in HM removal from wastewater are based on the ability of living organisms (plants, peat moss, bacteria, fungi, algae, etc.) to remove HMs from wastewater solutions (Figure 1-2). Toxic HMs affect the diversity and metabolic activities of living organisms. In turn, living organisms can overcome the stress from HMs and remove HMs through multiple strategies, such as sorption, precipitation, ion exchange, sequestration, etc. But the intrinsic interrelationship between the resistance to HMs and the HM removal ability of living organisms remains unclear. Different types of organisms show different properties in the process of HM removal utilizing their own bioremediation pathways.

Plant-based remediation methods, which are also called phytoremediation methods, have attracted increasing attention in the recent two decades [26]. The concept of using plants for HM removal was first proposed by Chaney in 1983 [35]. Basically, plants need to meet the demands of quick growth rate, well-developed root system, and strong adaptation to various habitats. Though the mechanisms of HM removal by plants are specific to different species, they generally include adsorption/absorption, sorption, precipitation, complexation, and volatilization by leaves. A great number of aquatic plants, such as water hyacinths, water lettuce, duckweed, and *Salvinia* sp., have shown their abilities to remove many kinds of HMs from wastewater [36-38].

The ability of peat moss to remove HMs from wastewater was first confirmed by several studies in the 1980s [39, 40], though this method has not been as widely investigated as other bioremediation methods. Peat moss is plentiful, inexpensive, and readily available. The mechanisms of HM removal by peat moss include ion exchange, surface adsorption, chemisorption, complexation, and adsorption-complexation. While it remains to be a controversial topic, ion exchange is the most prevalent mechanism [41].

Bacteria have been widely explored for HM removal in wastewater treatment by virtue of their abundance on earth (the most abundant organism on earth), strong adaptation in a wide range of environmental conditions, high aspect ratio (AR), quick

growth rate, and simple cultivation. The extracellular polymeric substances that consist of nucleic acids, proteins, lipids, complex carbohydrates [42], and the polysaccharide slime layers with many functional groups such as carboxyl, amino, phosphate, and sulfate groups [43], both play important roles in the adsorption of HMs. These adsorbed HMs can accumulate in the living bacterial cells and even further be changed to a state with lower toxicity through metabolism. Bacteria's ability to reduce HM toxicity can be used to further enhance their performance in HM removal. A series of bacteria, such as *Escherichia, Pseudomonas, Bacillus*, and *Ochrobactrum*, have been used for bioremediation of HMs [44-47].

Fungi have also been widely used to remove HMs since they were found to be able to live under high HM concentrations and accumulate HMs at the same time [48]. They, including macroscopic and microscopic (yeasts and molds) fungi, show the advantages of easy growth, high biomass yield, and easy morphological and genetic manipulation. Their high metal uptake ability is thought to be the result of abundant functional involved in HM biosorption, including the chitin-chitosan complex, glucuronic acid, phosphate, and polysaccharides in/on cells of fungi [49]. Fungi such as *Aspergillus niger*, *Aspergillus fumigatus*, *Termitomyces clypeatus*, *Saccharomyces cerevisiae*, and *Trichoderma* show good performance in removing different types of HMs such as Pb, Cr, Cu, Zn, and Cd [50-54].

An alga is a type of photosynthetic eukaryotic organism that can live in both freshwater (rivers, lakes, springs, and swamps) and seawater (salty lakes, seas, and oceans). It includes unicellular microalgae such as *Chlorella*, *Chlamydomonas*, and diatoms, and multicellular macroalgae, such as *Codium* and *Fucus*. Algae show good capability of removing HMs in wastewater and have been regarded as the most promising bio-sorbents because of their ready availability from almost all types of waterbodies, low nutrient requirement as they are autotrophic, shorter life span as compared to higher plants, and enormous biomass relative to any other microbial materials [33, 34, 55-57]. The mechanisms involved in HM removal include ion exchange, complexation, electrostatic attraction, and microprecipitation [58]. Although there are thousands of algal species, only a limited amount of them have been explored to remove HMs from wastewater. Many species remain unexplored for their capability of HM removal and much effort is being made to search for strains that show a high HM removal efficiency [33, 34, 55, 57].

Compared with macroalgal species, microalgal species are more promising in HM removal from wastewater because of their high AR, abundant biomass, and feasible cultivation. Microalgae serve as the largest group of primary producers in the world, which contribute to nearly one-third of global photosynthesis [59]. Presently, microalgae that have been studied for their ability to remove HMs include *Chlorella*, *Chlamydomonas*, *Euglena*, *Chaetoceros*, *Desmodesmus*, *Isochrysis*, *Planothidium*, *Scenedesmus*, *Spirulina*, etc. The mechanisms of HM removal by microalgae, the factors that affect their HM removal performance, as well as the methods used to improve their HM removal performance have been well studied [34].

## 1.3 Microalgae-based bioremediation methods

In recent decades, the use of microalgae in HM remediation has attracted increasing attention worldwide [34, 57]. Microalgae can live autotrophically in a wide range of water conditions through photosynthesis. They make great contributions towards reducing greenhouse gas carbon dioxide, which is the most notable advantage of microalgae over other microorganisms. Compared with macro plants, microalgae have much shorter life spans, which makes them easier to be investigated in the laboratory. Microalgae are used both in living and non-living types, and the performances of biomass in these two types are usually compared. It has been reported that living cells take up more HMs than dead biomass [34].

Many efforts have been made to investigate the HM removal mechanisms of various strains of microalgae. The mechanisms of removing HMs using microalgae are different for living and non-living microalgae, namely, bioaccumulation by living cells and biosorption by non-living biomass. For living cells, the accumulation process typically comprises three stages: (1) an initial rapid and passive adsorption of HMs by functional groups on the cell surface, (2) slow metabolism-dependent transportation across the cell membrane, and (3) accumulation inside the cell. In the first step, the functional groups on cell walls, including carboxyl (-COOH), amino (-NH$_2$), sulfhydryl (-SH), phosphate (-PO$_3$), and hydroxyl (-OH) groups facilitate coordination bonding with HMs. The different affinity of functional groups towards HMs leads to the specific binding. In the second step, the plasma membrane plays an important role in the membrane transport of HMs.

Specifically, membrane transporters are responsible for this process, which are categorized as group A and group B transporters [60]. Group A transporters can move HMs from the outside into the cytoplasm and group B transporters can decrease the HM concentration in the cytoplasm by mediating the exocytosis of excessive HMs. In the third step, metallothioneins (MTs), metallothionein-like proteins (MTLPs), Phytochelatins (PCs) are thought to be involved in the process of HM accumulation. MTs, which are small cysteine-rich proteins, as well as MTLPs, can bind HMs in stable complexes [61]. PCs are small metal-binding peptides synthesized from glutathione, homo-glutathione, hydroxymethyl-glutathione, or g-glutamylcysteine. They are able to form stable complexes with HMs. Besides these compounds, some cellular compartments also play an important role in HM accumulation, such as vacuoles, polyphosphate bodies, chloroplasts, and mitochondria. The mechanisms of HM removal by non-living microalgal biomass are much simpler, the biosorption through HM binding.

HM removal efficiency is a critical factor when evaluating an HM bioremediation method. As shown in Table 1-2, the HM removal efficiency of living microalgae varies greatly among species, ranging between 5.5% and nearly 99% with most of them below 90%. The factors of microalgal species, tolerance capacity, biomass concentration, size and volume of microalgae, pH, temperature, ion strength, salinity and hardness, and metal species all could affect the HM removal efficiency of microalgae, especially living ones [34]. And the above factors are different among the examples listed in Table 1-2. Therefore, it is impossible to compare the HM removal ability among these microalgal species simply based on their HM removal efficiency. Although a few microalgal species show HM removal efficiencies above 90% under laboratory conditions, it could be difficult to maintain such high HM removal efficiencies under practical wastewater treatment conditions. Also, compared with the conventional physico-chemical methods, it usually takes a much longer time for microalgae to remove HMs. Generally, the time taken by microalgae to remove HMs is over one day. The low removal efficiency seriously hinders the practical implementation of microalgae for HM removal in wastewater treatment.

Table 1-2. HM removal using living microalgae

| HM | Microalgal species | Initial concentration of HM (mg/L) | Removal efficiency | Exposure time (h) | Reference |
|---|---|---|---|---|---|
| Cu$^{2+}$ | *Anabaena cylindrica* | 0.45 | 50% | 1 | [62] |
| | *Chlorella pyrenoidosa* | 0.05 | 95% | 144 | [63] |
| | *Closterium lunula* | 0.05 | 79% | 144 | [63] |
| | *Scenedesmus obliquus* | 0.05 | 67% | 144 | [63] |
| | *Euglena gracilis* | - | 58% | 5 | [64] |
| | *Chlamydomonas reinhardtii* | 0.03 | 28% | 1 | [65] |
| Ni$^{2+}$ | *Euglena gracilis* | - | 44% | 5 | [64] |
| | *Chlorella vulgaris* | 30 | 56.7% | 5 | [66] |
| | *Scenedesmus quadricauda* | 30 | 99.0% | 5 | [66] |
| | *Chlorella sorokiniana* | 30 | 53.3% | 5 | [66] |
| Cd$^{2+}$ | *Desmodesmus pleiomorphus* (L) | 5 | 52.6% | 168 | [67] |
| | *Desmodesmus pleiomorphus* (ACOI 561) | 5 | 53.9% | 168 | [67] |
| | *Desmodesmus pleiomorphus* (L) | 0.5 | 98.8% | 168 | [67] |
| | *Desmodesmus pleiomorphus* (ACOI 561) | 0.5 | 98.1% | 168 | [67] |
| | *Euglena gracilis* (Z) | 11.1 | 13% | 96 | [68] |
| | *Euglena gracilis* (Z-Hg$^{2+}$) | 11.1 | 12% | 96 | [68] |
| | *Euglena gracilis* (ZL) | 11.1 | 16% | 96 | [68] |

| | | | | | |
|---|---|---|---|---|---|
| | *Euglena gracilis* (ZL-Hg$^{2+}$) | 11.1 | 29% | 96 | [68] |
| | *Pseudochlorococcum typicum* | 3.3 | 76% | 24 | [69] |
| | *Euglena gracilis* | 2.2 | 80% | 192 | [70] |
| | *Chlamydomonas reinhardtii* CC-425 | 4.5 | 5.5% | 120 | [71] |
| | *Chlamydomonas reinhardtii* pMTCC-8 | 4.5 | 9% | 120 | [71] |
| Hg$^{2+}$ | *Pseudochlorococcum typicum* | 7.0 | 98% | 24 | [69] |
| Pb$^{2+}$ | *Chlamydomonas reinhardtii* | 0.1 | 8% | 1 | [65] |
| | *Pseudochlorococcum typicum* | 3.3 | 62% | 24 | [69] |
| | *Oscillatoria laete-virens* | 10 | 28% | 24 | [72] |
| | *Oscillatoria laete-virens* | 80 | 11% | 24 | [72] |
| | *Spirulina (Arthrospira) platensis* | 5 | 31% | 720 | [73] |
| | *Spirulina (Arthrospira) platensis* | 100 | 56% | 720 | [73] |

Presently, research into improving the HM removal efficiency of living microalgae has been scarcely investigated [56, 68, 74-79]. Table 1-3 shows some examples of the methods used to improve HM removal efficiency of microalgae and their performance. For instance, immobilization of microalgal cells using biomaterials such as alginate and loofa sponge has been shown to effectively boost the HM removal ability of microalgae [74, 75, 79]. The enhanced HM removal efficiency is mainly a result of increased surface area and free access of the HMs to sorption sites. But the reachable HM removal efficiency is limited by that of the microalgal cells themselves. Pretreatment of microalgal

cells through changing cultivation conditions (such as high-phosphate culture-modification and mercury pretreatment) has also been performed [68, 76, 78]. The increased surface functional groups or cellular PCs contribute to the enhanced HM removal efficiency. But its effect on HM removal efficiency is insufficient for practical use in wastewater treatment. In addition to these methods, the development of new microalgal species is attractive because it can improve the intrinsic HM removal capability of microalgae. Genetic modification of microalgae, so as to contain the targeted gene sequences, has been demonstrated for developing microalgae with an enhanced HM removal efficiency, provided that the desirable gene sequences are known [56, 71, 77, 80]. However, there is a barrier to deploying genetically modified species in real-world environments due to its potential threat to human health. Also, at present, genetic modification of microalgae is successfully only using the model system of *Chlamydomonas reinhardtii* due to the lack of commercially available kits for nuclear and chloroplast transformation for other species. A novel method to develop a new microalgal species without the potential threat to human health is needed to greatly improve the HM removal efficiency of microalgae and thus promote the utilization of microalgae-based bioremediation methods for practical HM removal in wastewater treatment.

Table 1-3. Ability of the methods to improve HM removal efficiency of microalgae

| Method | Microalgal species | HM | Percentage of improvement | Reference |
|---|---|---|---|---|
| Immobilization by loofa sponge | *Chlorella sorokiniana* | $Pb^{2+}$ | 124% | [74] |
| High-phosphate culture-modification | *Chlorella* sp. | $Pb^{2+}$ | 413% | [78] |
| High-phosphate culture-modification | *Scenedesmus obtusus* | $Hg^{2+}$ | 149% | [76] |
| Mercury pretreatment | *Euglena gracilis* | $Cd^{2+}$ | 154% | [68] |
| Genetic modification | *Chlamydomonas reinhardtii* | $Cd^{2+}$ | ~ 300% | [77] |
| Genetic | *Chlamydomonas* | $Cd^{2+}$ | 164% | [71] |

| modification | *reinhardtii* | | | |
|---|---|---|---|---|
| Genetic modification | *Chlamydomonas reinhardtii* | $Cd^{2+}$ | 416% | [80] |

## 1.4 Directed evolution of microalgae

Directed evolution, which is performed through multiple rounds of mutagenesis, selection, and amplification (Figure 1-3), is a promising method for developing microalgae with a much higher HM removal efficiency for mainly two reasons. First, it can be performed without a comprehensive gene annotation and the requirement of commercially available kits for nuclear and chloroplast transformation, thus is much simpler than the genetic modification method and applicable to many microalgal species. Also, directed evolution does not have the regulatory problems of using new strains in wastewater treatment systems, which is hence advantageous over the genetic modification method. Directed evolution has been widely employed for discovering superior enzymes and strains, especially when combined with the rapidly developing techniques of machine learning and high-throughput screening [81-83]. This method has been successfully used to select some bacteria like *Escherichia coli* with improved performance [84, 85]. Currently, however, directed evolution is yet to be applied for the selection of microalgae with enhanced performance in HM removal.
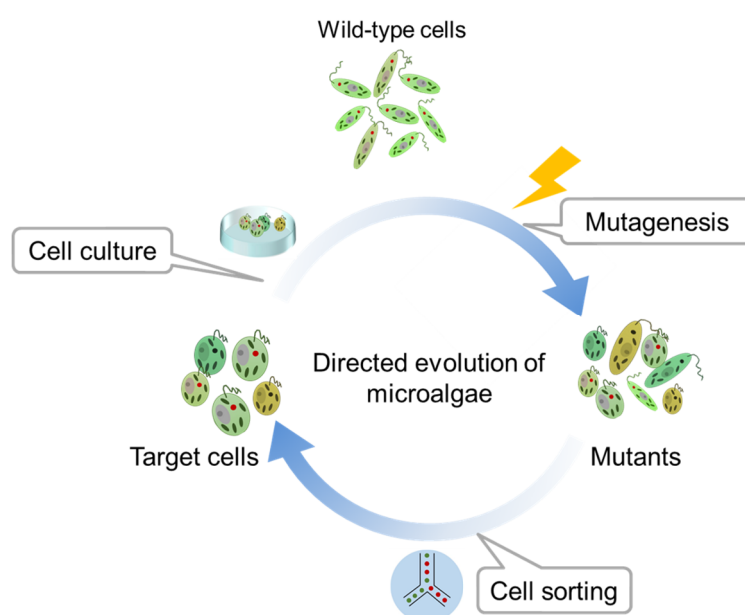


Figure 1-3. The overall directed evolution procedure of microalgae. It consists of three steps: (1)

mutant generation through random mutagenesis; (2) rare target cell isolation from the mutants through single-cell sorting; (3) cell proliferation through cell culture.

It is challenging to experimentally demonstrate the directed evolution of microalgae with improved HM removal efficiency because a measurable indicator of HM in the cells is required to identify the highly efficient cells in the cell selection step. Furthermore, this indicator should be non-invasive and label-free to avoid toxicity for the microalgal cells. In fact, there are currently multiple indicators representing the HM removal efficiency at a single-cell level, but they are not applicable to directed evolution because either their invasive or labelling is required. An example of the invasive indicators is the ion intensity of HMs within each cell, which can be measured directly using single-cell inductively coupled plasma mass spectrometry [86, 87] with the cost of destruction of the cells. An example of the label-requiring indicators is the fluorescence intensity of metal fluorescent probes [88-90], but there is a risk of interfering with cellular functions [91]. To the best of my knowledge, there are no non-invasive or label-free indicators to identify microalgal cells with their HM removal efficiency.

Benefiting from the development of high-speed single-cell imaging technologies [92-94], rich cellular morphological information could be obtained easily and rapidly in a non-invasive and label-free manner [95-97]. For instance, single-cell morphology can be used to classify platelet aggregates, test drug susceptibility of leukemia, predict DNA content, analyze cell cycle, and select human sperm with high DNA integrity [95-98]. The ability of cellular morphology to indicate microalgal HM removal efficiency has not been studied yet. It is of great significance to investigate whether cellular morphology could be an effective indicator of the HM removal efficiency of microalgae because it can be detected in a way without any damage to cells or interference with cellular functions, which is critical for an indicator used in directed evolution. If the cellular morphology can indicate the HM removal efficiency of microalgae, it will have great potential, when combined with a high-throughput image-activated cell sorter [99-104], for directed-evolution-based development of *E. gracilis* with an extremely high HM removal efficiency for practical wastewater treatment worldwide.

## 1.5 Goal of this thesis

The goal of this thesis is to propose and experimentally demonstrate an intelligent cellular morphological indicator for non-invasive and label-free identification of the HM removal efficiency of microalgae, to realize the directed evolution-based development of microalgae with extremely high HM removal efficiency for practical wastewater treatment in the future. Specifically, a model microalgal species of *E. gracilis* is used, which is an industrially attractive microalgal species that has been recognized to remove various types of HMs such as Cu [64, 105], Cd [68, 70, 106-108], Pb [70, 108], Zn [70, 105], Ni [64, 109], Cr [110], As [111], and Hg [108]. $Cu^{2+}$ is used as a model HM because it is one of the most toxic HMs in wastewater and is known to cause serious health problems in animals and humans if its concentration is excessive [112]. To verify this identification method, I perform the following five steps: (1) preparation of clones derived from single *E. gracilis* cells; (2) imaging flow cytometry of the *E. gracilis* clones under $Cu^{2+}$ exposure; (3) extraction of their morphological features using machine learning; (4) measurement of the $Cu^{2+}$ removal efficiency of each clone by analyzing the change in the $Cu^{2+}$ concentration in its culture medium; and (5) analysis of the correlation between the morphological features and $Cu^{2+}$ removal efficiency of the *E. gracilis* clones. It is expected that the morphological features are highly correlated with $Cu^{2+}$ removal efficiency of the *E. gracilis* clones, thus enabling the intelligent morphological indicator to be used in the improvement of the HM removal efficiency of microalgae through directed evolution and providing a highly efficient, sustainable, eco-friendly, and low-cost bioremediation method for HM removal in wastewater treatment.

# Chapter 2

# Materials and methods

## 2.1 Overview

To demonstrate a morphological indicator of microalgal HM removal efficiency, a model microalgal species, *E. gracilis*, and a model HM, $Cu^{2+}$ are used. The preparation of clones derived from single *E. gracilis* cells, a method for high-throughput single-cell imaging, a method for analyzing morphological features, and a method for measuring $Cu^{2+}$ removal efficiency are required. In addition, to evaluate cellular activity in each clone, it is necessary to check cell growth rate, viability, and nutrient consumption. In this chapter, I will introduce the details of these materials and methods.

## 2.2 Procedure for studying the correlation between the morphology and $Cu^{2+}$ removal efficiency of *E. gracilis*

The procedure for studying the correlation between the morphology and $Cu^{2+}$ removal efficiency of *E. gracilis* consists of five steps (see Figure 2-1). First, single cells from an original *E. gracilis* strain are isolated in a 96-well plate with a working volume of 200 μL and cultured until each of the clones derived from single cells reaches its stationary phase. Then, these clones are transferred into a flask for culturing, subculturing, and culturing again to maintain the clones in the logarithmic phase with a working volume of 20 mL. Second, single-cell images of each clone exposed to 0 μM (as a control), 5 μM (not shown in Figure 2-1), or 7.5 μM $Cu^{2+}$ are acquired by high-throughput imaging flow cytometry using optofluidic time-stretch microscopy [92-94, 97, 113-118]. Third, the cellular morphological features of each clone are analyzed using machine learning. Fourth, the $Cu^{2+}$ removal efficiency of each clone is evaluated by measuring and analyzing the change in $Cu^{2+}$ concentration in the medium after adding 7.5 μM $Cu^{2+}$ to the culture medium of each clone and culturing them for 72 h. All samples are cultured under the same conditions before and during $Cu^{2+}$ exposure so that clone differences can be evaluated without bias. Fifth, the morphological features (under 0 and 7.5 μM $Cu^{2+}$

exposure) and $Cu^{2+}$ removal efficiency of the clones are plotted to investigate the potential correlation between them. If the morphological features of clones show a strong correlation with $Cu^{2+}$ removal efficiency, it means that the morphological features can be effective indicators of $Cu^{2+}$ removal efficiency.
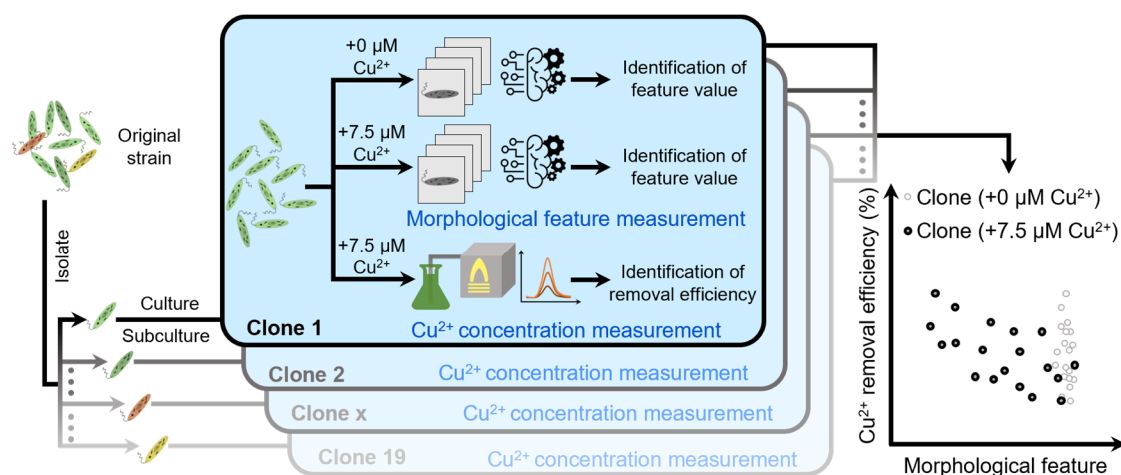


Figure 2-1. Schematic of the workflow for identifying the correlation between the morphology and $Cu^{2+}$ removal efficiency of *E. gracilis*. It consists of five steps: (1) preparation of 19 clones derived from single *E. gracilis* cells; (2) imaging flow cytometry of the 19 *E. gracilis* clones under $Cu^{2+}$ exposure; (3) extraction of their morphological features using machine learning; (4) measurement of the $Cu^{2+}$ removal efficiency of each clone by analyzing $Cu^{2+}$ concentration change in its culture medium; (5) analysis of the correlation between the morphological features and $Cu^{2+}$ removal efficiency of the *E. gracilis* clones. Reproduced with permission from ref [119]. Copyright 2021 American Chemical Society.

## 2.3 Cell culture and clone preparation

The procedures for cell culture and clone preparation are shown in Figure 2-2. I used *E. gracilis* NIES-48 provided by the Microbial Culture Collection at the National Institute for Environmental Studies (NIES) as the original strain. It is a green unicellular microalgal species living in fresh water. The surface of *E. gracilis* cells is highly flexible that allows the cells to swim and adjust their shape between elongated and spherical shapes. The length and width of *E. gracilis* cells are around 40 μm and 10 μm, respectively (see Figure 2-3). The cultures were grown under 14:10 light:dark cycle illumination (warm white, 130-150 μmol/m$^2$/s) at 25 °C (see Figure 2-4). The 14:10

light:dark cycle illumination aided the life cycle of *E. gracilis* cells to be regulated, thus maintaining the life cycle of cells synchronized. For all experiments, the stock culture of *E. gracilis* was grown in an autotrophic medium, AF-6 (see ref. [120] for details of components and their concentrations). After the sample preparation, I used a fluorescence-activated cell sorting (FACS) machine (BD FACS Aria III, BD Biosciences, USA) to isolate single cells from the original *E. gracilis* strain into a 96-well plate. Using FACS is much more efficient for obtaining dozens of clones in a single 96-well plate than using a serial dilution method because it guarantees that single cells are seeded in all 96 wells within several minutes. To achieve this, cell suspensions were identified from empty suspensions by measuring the autofluorescence of *E. gracilis* cells (excitation wavelength = 633 nm, emission wavelength = 660 nm). After culturing these single cells of *E. gracilis* in the same AF6 medium with a working volume of 200 μL under the same conditions mentioned above for 14 days, I obtained 32 clones (see Figure 2-5). The ratio of clones successfully grown from the survived single cells varies depending on experimental conditions. Then, each of the clones was transferred to a flask with a working volume of 10 mL, cultured for 4 days, and subcultured in 20 mL of AF-6 with an initial concentration of $1.5 \times 10^3$ cells/mL for another 4 days so that the final cell concentration reached ~2.5 $\times 10^4$ cells/mL. The cells were in the logarithmic phase when they were exposed to $Cu^{2+}$ after being cultured for 22 days, as demonstrated in Figure 2-6 that shows the cell concentration of each clone along time. The cell cycle was synchronized because the cells in the synchronized conditions (in logarithmic phase, under 14:10 light:dark cycle illumination) show an overall more uniform distribution in morphology when compared with the non-synchronized cells (see Figure 2-7). Among these clones, I randomly selected 19 clones and numbered them for further experiments.
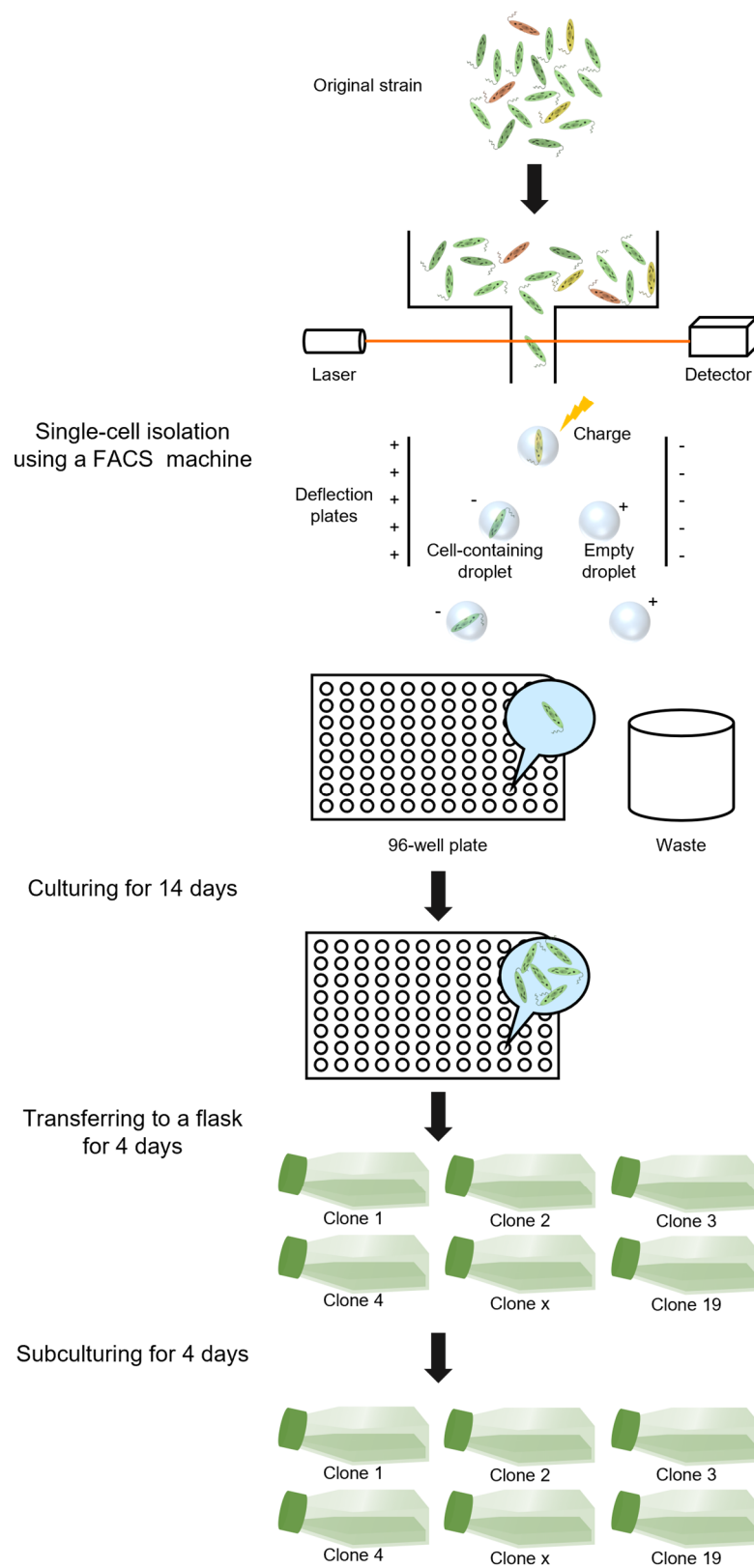
Figure 2-2. Workflow of cell culture and clone preparation.
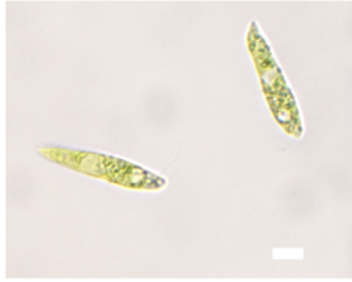
Figure 2-3. Bright-field image of two *E. gracilis* cells. Scale bar: 10 μm.
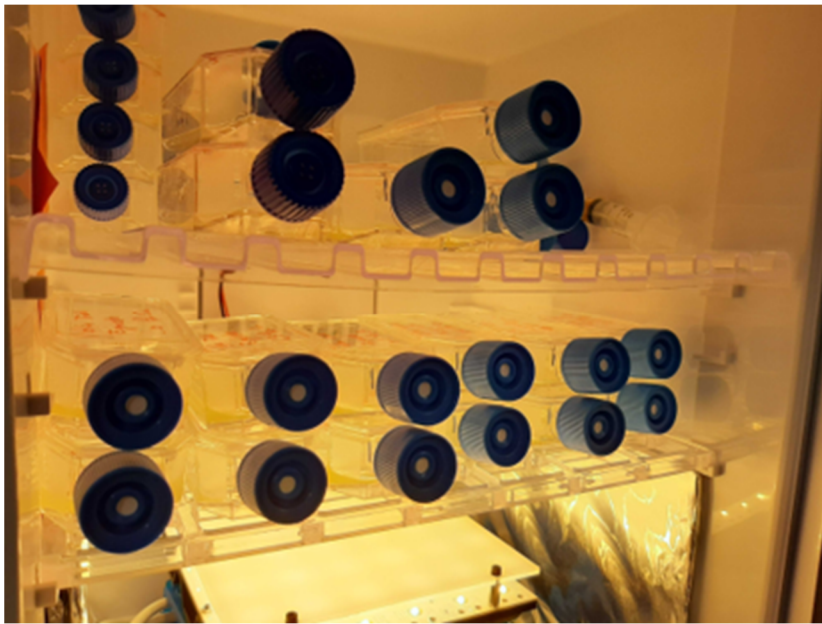


Figure 2-4. *E. gracilis* cultured in flasks in an incubator.
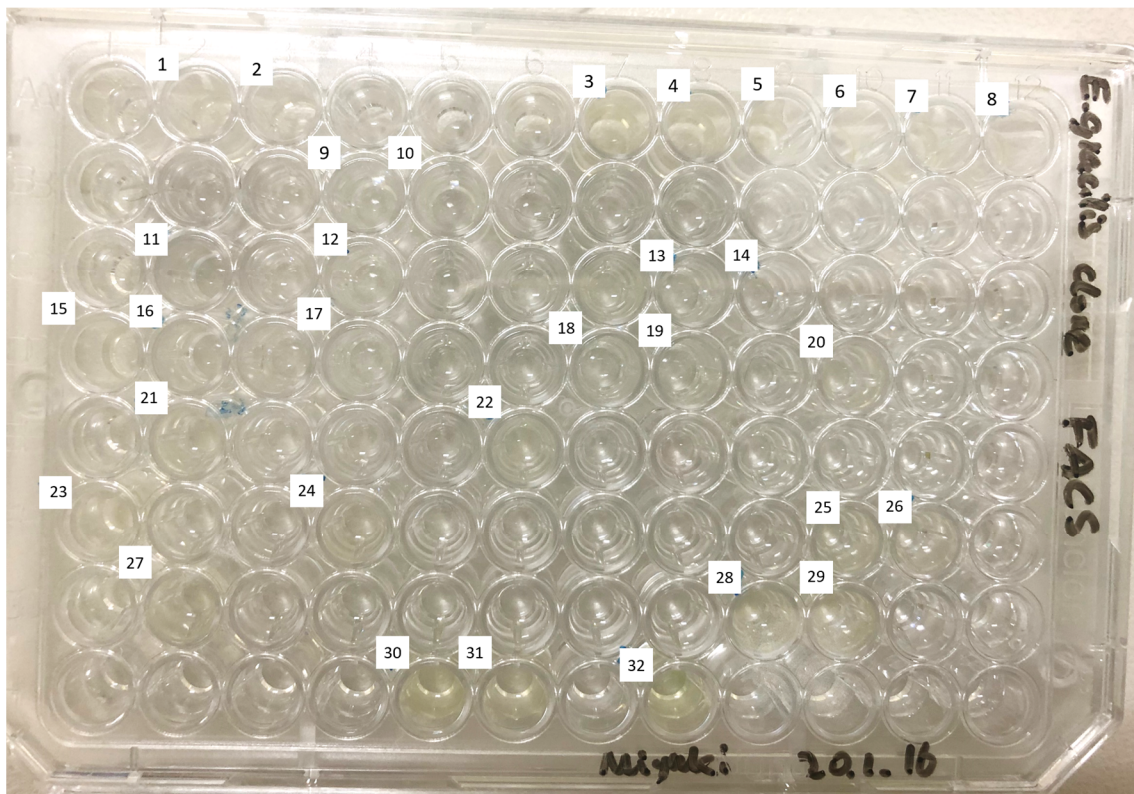
Figure 2-5. 96-well plate containing 32 clones deriving from single *E. gracilis* cells. Wells that contain clones derived from single *E. gracilis* cells are labelled with numbers (top left corner).
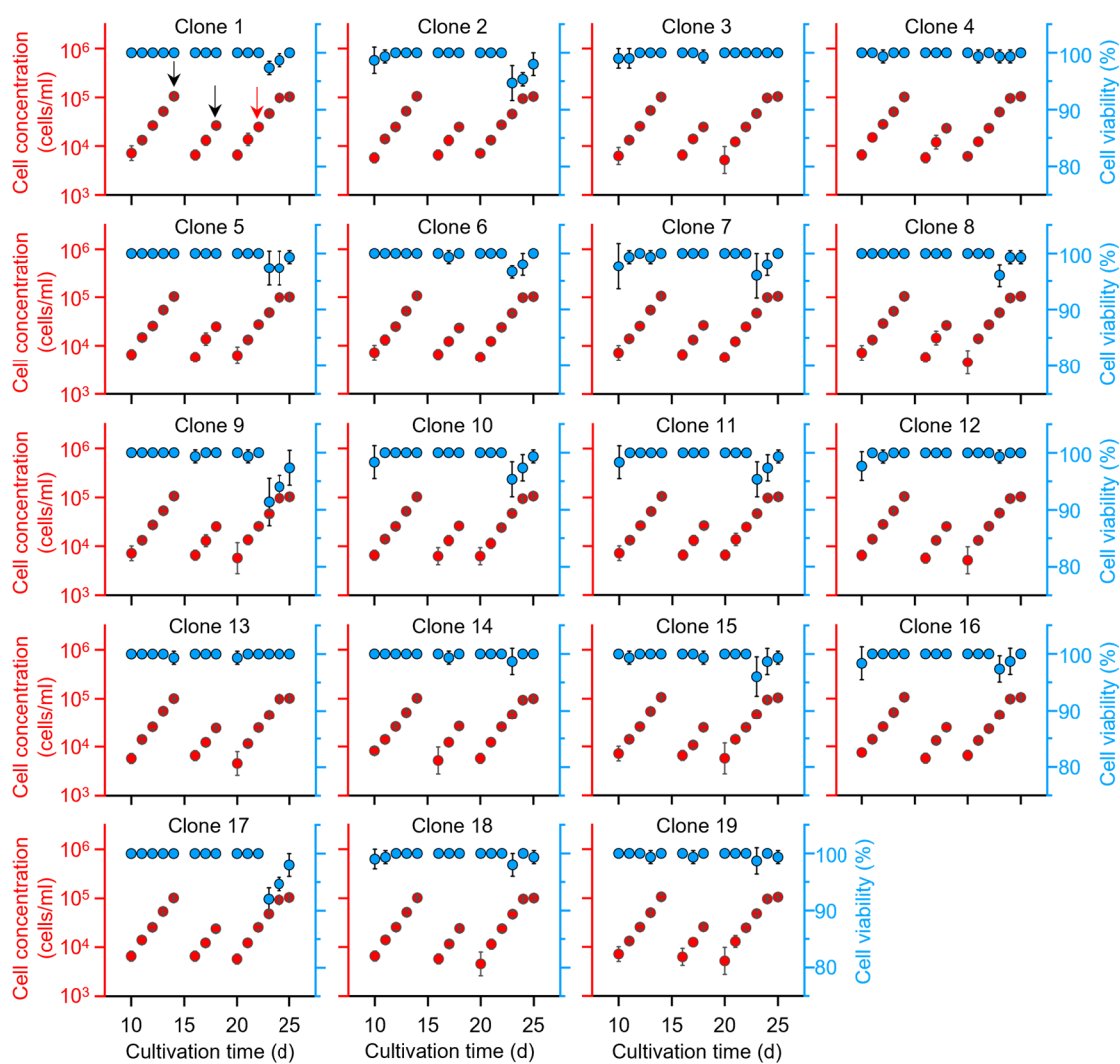
Figure 2-6. Cell concentration and viability of all *E. gracilis* clones in the preparation steps and exposure experiments. The black arrows and a red arrow in the graph for Clone 1 represent the subculture timings and exposure timing, respectively. The error bars represent standard deviations of cell concentrations and cell viabilities (n = 3 measurements). Reproduced with permission from ref [119]. Copyright 2021 American Chemical Society.
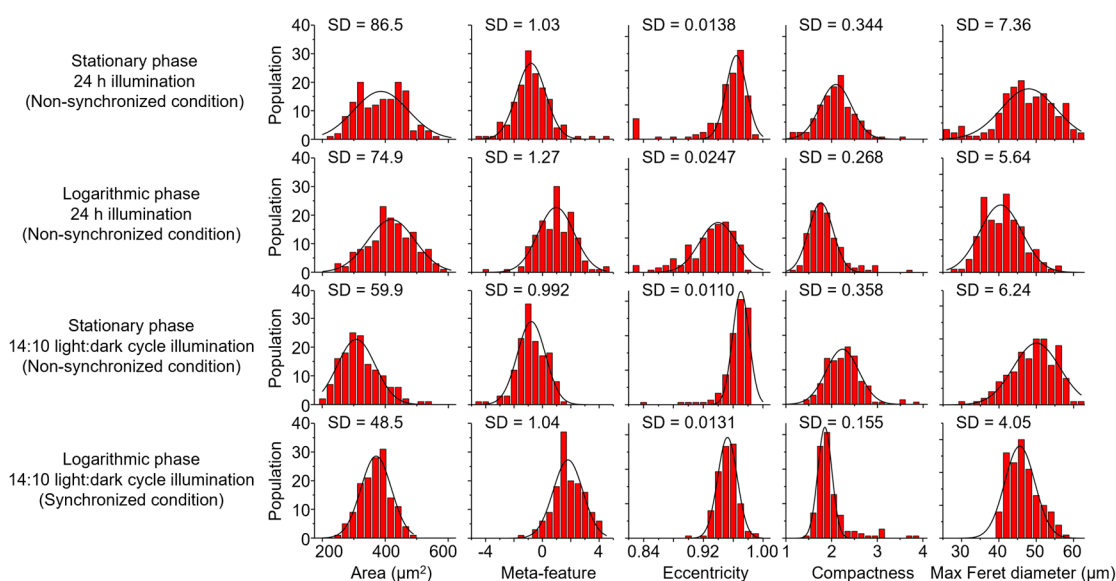
Figure 2-7. Cell area, morphological meta-feature, eccentricity, compactness, and max Feret diameter value distributions under various culture conditions. The projected area in a two-dimensional image taken by the optofluidic time-stretch microscope was used as the cell area. N = 144 images. Reproduced with permission from ref [119]. Copyright 2021 American Chemical Society.

## 2.4 Imaging flow cytometry by optofluidic time-stretch microscopy

To acquire hundreds of single-cell images of *E. gracilis* for all experimental groups (one original strain and 19 clones, each sample under three $Cu^{2+}$ exposure conditions), a high-speed single-cell imaging technique was needed. The single-cell images of *E. gracilis* were taken by high-throughput imaging flow cytometry based on optofluidic time-stretch microscopy. Optofluidic time-stretch microscopy is a powerful technology to acquire highly qualified bright-field single-cell images at a high speed. It is capable of providing blur-free bright-field images of single cells at an ultrahigh throughput of 100,000 cells per second [92, 94, 96, 114, 116]. There are two main technologies involved: optical time-stretch imaging and hydrodynamic focusing. Optical time-stretch imaging is the fundamental technology for high-speed imaging while hydrodynamic focusing is critical for aligning cells in a microfluidic channel on the focal plane as they are flowing at a high speed. The principles of these two technologies will be discussed as follows.

Optical time-stretch imaging is a technique that maps the spatial information into the spectrum of an ultrafast broadband optical signal that is temporarily stretched [118]. The reason for stretching the optical signal in the time domain is to optimize the signal

acquisition condition and enable detection of the spatial information encoded in the pulse, overcoming the speed and resolution limitations of electronic digitizers. The process of optical time-stretch imaging requires two steps of transformation: first, frequency-to-space transformation to encode the spatial profile of the imaging target in the frequency domain, and second, frequency-to-time transformation to enable the temporal detection of the spectrum by a single-pixel photodetector [118].

The microfluidic chip plays an important role in the optofluidic time-stretch microscopy because it allows constant and high-speed flowing of cells while aligning them in the optical focal plane and field-of-view at the same time. In order to meet these requirements, hydrodynamic focusing is used in imaging flow cytometry. It is a technique that uses a sheath flow to encompass the sample flow to achieve good focusing of the sample flow in the field-of-view by the effect of fluid dynamics (Figure 2-8). By tuning the flow-rate ratio of the sheath and sample flows, it is easy to control the cross-sectional area of the focused sample flow. Usually, this ratio is set at a pretty high value to keep the sample flow well focused at the center of the channel.
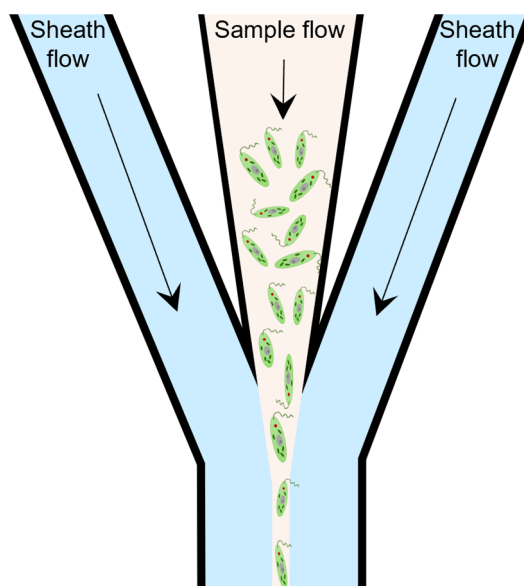


Figure 2-8. Two-dimensional hydrodynamic focusing of flowing *E. gracilis* cells into a single stream.

The schematics of an optofluidic time-stretch microscope and a microfluidic chip used with it used in this thesis are shown in Figures 2-9A and 2-9B. The photographs of them are shown in Figures 2-9C and 2-9D. The optical setup and process to acquire single-

cell images of *E. gracilis* are the same as those in previously reported literature [92-94, 97, 113-118]. The microscope mainly consists of a pulse laser, a dispersion fiber, two diffraction gratings, two objective lenses, a microfluidic chip, and a high-speed photodetector and functions as follows. A pulse from the Ti:Sapphire mode-locked femtosecond pulse laser (center wavelength: 790 nm, bandwidth: 40 nm, pulse repetition rate: 75 MHz) is temporally stretched by the dispersion fiber with a dispersion amount of -240 ps/nm and then spatially dispersed by the first diffraction grating with a groove density of 1,200 lines/mm. This spatially dispersed pulse is focused by the first objective lens, which has a numerical aperture and magnification of 0.6 and 40×, respectively, onto the microchannel on the microfluidic chip (Figure 2-9B). Thus, the spectrum of the transmitted pulse contains the one-dimensional (1D) spatial profile of a flowing *E. gracilis* cell in the microchannel. This transmitted pulse is collected by the second objective lens with the same numerical aperture and magnification and spatially recombined by the second diffraction grating with the same groove density. Finally, the recombined pulse is detected by a high-speed photodetector with a detection bandwidth of 12 GHz. Since each pulse contains the 1D image of the flowing *E. gracilis* cell in the y direction (orthogonal to the flow direction of the cells) (Figure 2-9B), a two-dimensional (2D) image of the *E. gracilis* cell can be obtained by digitally stacking the 1D image profiles in the x direction. 2D images were reconstructed on MATLAB R2016b following the same procedure as previously reported [94].

The microfluidic chip used with the microscope (Figure 2-9D) is designed and fabricated in the same way as previously reported [94]. The dimensions of the microchannel are 60 mm (along the x axis), 80 μm (along the y axis), and 40 μm (along the z axis). Flowing cells are focused into a single stream by a hydrodynamic cell focuser consisting of a sheath flow and sample flow. The flow rates of the sheath flow and the sample flow were set to 0.6 mL/min and 0.06 mL/min, respectively, for high focusing performance and high flow speed of *E. gracilis* cells (~5 m/s).
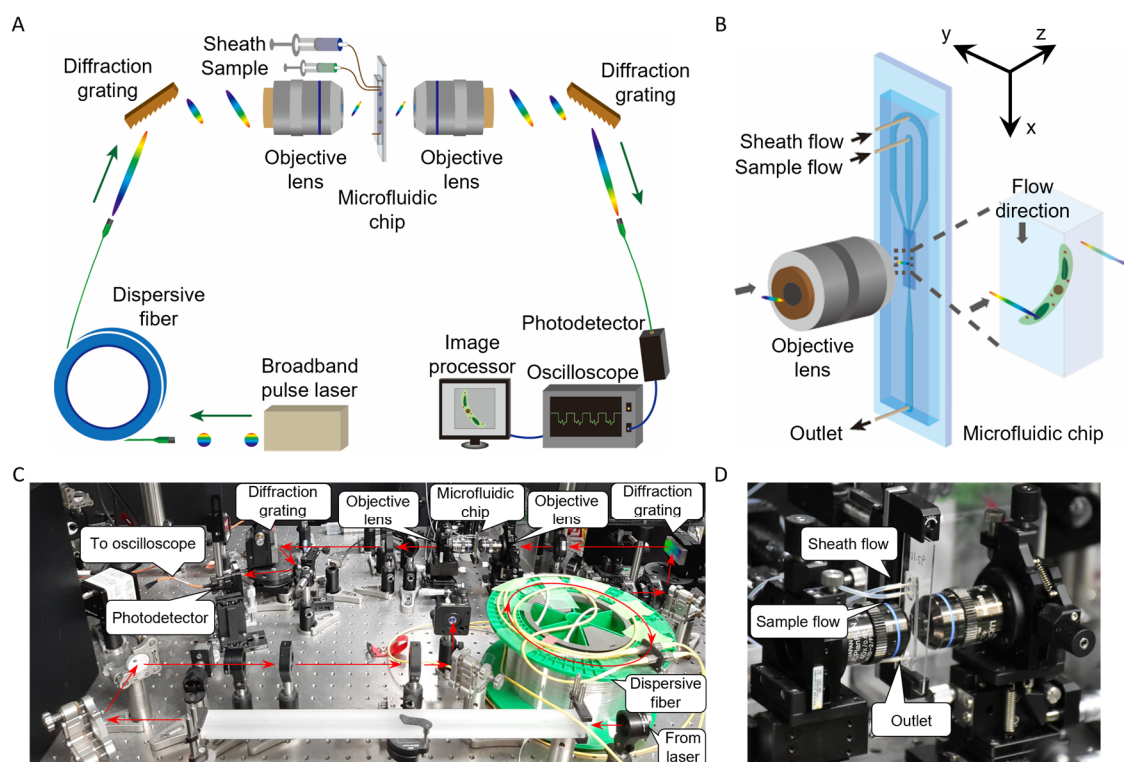
Figure 2-9. High-throughput imaging flow cytometry of *E. gracilis* cells. (A) Schematic of the optofluidic time-stretch microscope. (B) Microfluidic chip in the microscope. (C) Photograph of the optofluidic time-stretch microscope. (D) Photograph of the microfluidic chip used with the microscope. Reproduced with permission from ref [119]. Copyright 2021 American Chemical Society.

## 2.5 Extraction and evaluation of morphological feature by machine learning

To find out the most distinct morphological features among the clones derived from single *E. gracilis* cells, it is necessary to extract their morphological features and classify them by machine learning for the evaluation of the weight of these morphological features on classification. The workflow of the morphological feature extraction and evaluation is shown in Figure 2-10. In this section, I introduce the principle of morphological feature extraction and evaluation by machine learning.
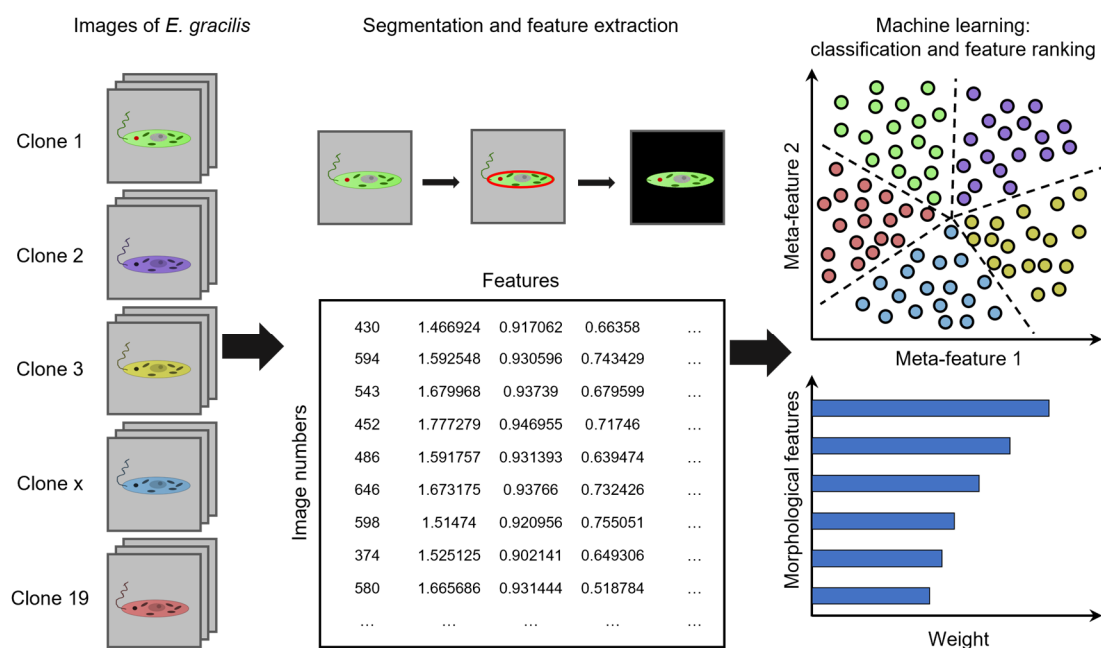
Figure 2-10. Workflow of morphological feature extraction and evaluation.

Morphological feature extraction is necessary because the cellular images of *E. gracilis* can not be used directly in machine learning. It is a method to process images by using mathematical algorithms and output a series of morphological feature values associated with the input image. Morphological features can be extracted by using various methods, such as MATLAB, Python, ImageJ, and CellProfiler. The use of MATLAB and Python requires programming expertise. ImageJ and CellProfiler are both free and open-source software without the requirement of programming expertise. ImageJ is more applicable for the analysis of individual images or image stacks. In comparison, CellProfiler is powerful for the quantitative analysis of hundreds or thousands of images simultaneously. It has been employed to extract human-interpretable features with biological meaning [95, 121, 122]. Therefore, CellProfiler is used for the morphological feature extraction from hundreds of single-cell images of the original strain and 19 *E. gracilis* clones. To extract morphological features from the single-cell images obtained by the optofluidic time-stretch microscopy, the objective area of each *E. gracilis* cell is first segmented based on a mean correlation threshold in CellProfiler. Second, morphological feature values, including values of morphological features related to the cell size, shape, intensity distribution, and orientation are extracted from the corresponding segmented cell image.

Using these obtained morphological feature values, the morphological features can be ranked based on their weight to classification via a sequential minimal optimization support vector machine (SVM) [123, 124] with a polynomial kernel. SVM is a supervised learning model in data analysis for classification and regression analysis by using associated learning algorithms. It can be performed by WEKA (Waikato Environment for Knowledge Analysis) [125], a free software program for machine learning. To avoid overfitting, the performance of the SVM is measured with 10-fold cross-validation, which is a resampling procedure used to evaluate machine learning models. The weight of the morphological features obtained by the SVM indicates the contribution of these morphological features to the classification. The higher the weight of a morphological feature, the more contribution the morphological feature has to the classification. Finally, a morphological meta-feature that optimally classifies the clones can be developed by conducting a linear combination of the SVM-identified morphological features. Linear discriminant analysis (LDA) is used to reduce the dimensionality of the morphological features into a single meta-feature.

## 2.6 Measurement of $Cu^{2+}$ removal efficiency

The $Cu^{2+}$ removal efficiency of each clone was evaluated by measuring the change of the remaining $Cu^{2+}$ concentration in its culture medium using inductively coupled plasma atomic emission spectrometry (ICP-AES) (iCAP 6300, Thermo Fisher Scientific, Germany). The whole procedure consists of four steps. First, each culture was exposed to 7.5 μM $Cu^{2+}$ and cultured for 72 h. Here, I cultured cells for 72 h, which is the typical exposure time for evaluating the HM removal efficiency of microalgae [126-128]. Second, after 72 h, the supernatant of each culture was collected by centrifuging at 3,000g for 5 min. Third, the $Cu^{2+}$ concentration of the supernatant ($C_{sample}$) was measured by ICP-AES. For the control, a fresh culture medium (AF6) with no cell suspension was treated with the same concentration of $Cu^{2+}$ for 72 h. Then, its $Cu^{2+}$ concentration was measured by ICP-AES ($C_{control}$). Finally, the $Cu^{2+}$ removal efficiency was calculated by 1-($C_{sample}/C_{control}$).

## 2.7 Evaluation of cell growth rate, viability, and nitrogen consumption

To understand the effect of $Cu^{2+}$ exposure on cell activities, some important physiological parameters such as cell growth rate, cell viability, and nutrient consumption were evaluated. The cell concentration of each clone was measured with a hemocytometer and then the cell growth of each clone was calculated as the number of cells 72 h after $Cu^{2+}$ exposure divided by the number of cells before $Cu^{2+}$ exposure. The viability of each clone was determined by staining cells with 0.025% (w/v) trypan blue. To evaluate nutrient consumption, I evaluated the amount of nitrogen (an important nutritional source in AF6 medium) consumed by each clone by measuring the remaining nitrogen source (nitrate-nitrogen and ammonium-nitrogen) concentration in its culture medium. The procedure of the nitrogen concentration measurements consists of four steps. First, the supernatant of each culture before $Cu^{2+}$ exposure and 72 h after $Cu^{2+}$ exposure was collected by centrifuging at 3,000g for 5 min. Second, nitrate-nitrogen concentration ($C_{nitrate0}$ for that before $Cu^{2+}$ exposure and $C_{nitrate72}$ for that 72 h after $Cu^{2+}$ exposure) was determined by measuring the absorption at a wavelength of 220 nm with an ultraviolet absorption spectrometer (JASCO, V-730) following the same procedure as previously reported [129]. Third, ammonium-nitrogen concentration ($C_{ammonia0}$ for that before $Cu^{2+}$ exposure and $C_{ammonia72}$ for that 72 h after $Cu^{2+}$ exposure) was measured using a LabAssay TM Ammonia kit (FUJIFILM Wako Pure Chemical Corporation, Japan) following the detailed testing protocol enclosed with the kit. Briefly, the supernatant of each culture was stained with three chromogens in the kit, followed by measuring the absorption at a wavelength of 630 nm. Finally, the nitrogen consumption was obtained by calculating $[(C_{nirate0} + C_{ammonia0}) - (C_{nitrate72} + C_{ammonia72})]/(C_{nirate0} + C_{ammonia0})$.

# Chapter 3

# Experimental demonstration of morphological indication

## 3.1 Overview

As mentioned in Chapter 1, morphological features have the potential to be a non-invasive and label-free indicator of microalgal HM removal efficiency should these two variables proved to be highly correlated. In this chapter, I describe the experimental demonstration of the capability of morphological features to be effective indicators of microalgal HM removal efficiency. Specifically, I describe the single-cell images of the original strain and 19 clones obtained using imaging flow cytometry, top-ranked morphological features, $Cu^{2+}$ removal efficiency of $E.$ $gracilis$, the correlation between morphological features and $Cu^{2+}$ removal efficiency, and cellular activity of the original strain and 19 clones.

## 3.2 Imaging flow cytometry of $E.$ $gracilis$ clones under $Cu^{2+}$ exposure

To study the potential effect of $Cu^{2+}$ exposure on the morphology of $E.$ $gracilis$ cells and clone-to-clone differences, I used optofluidic time-stretch microscopy [92-94, 97, 113-118] to perform high-throughput imaging flow cytometry of single $E.$ $gracilis$ cells of the original strain and 19 single-cell derived clones under a range of $Cu^{2+}$ exposure conditions (0, 5, and 7.5 μM $Cu^{2+}$). Figure 3-1 shows 20 single-cell images (randomly selected from 144 images) of the original strain and two clones under each $Cu^{2+}$ exposure condition. These two clones were "Clone 9" and "Clone 19" shown in Figure 3-2. As shown in Figure 3-1, the cells from the original strain were morphologically heterogeneous under $Cu^{2+}$ exposure. In contrast, the cells from Clone 9 and Clone 19 displayed different morphological changes even though their $Cu^{2+}$ exposure conditions were identical, while the cells within each clone had a consistent response. Specifically, without the $Cu^{2+}$exposure, all of the imaged 144 cells of the original strain and 19 clones (partially shown in Figure 3-1 and 3-2) had an elongated shape with a high AR. Diverse changes in cellular morphology of the original strain were observed after exposure to 5 μM $Cu^{2+}$;

some of the cells changed their elongated shape to a spindled shape with a smaller AR, while the others remained unchanged. This cell-to-cell heterogeneity in morphology became more apparent after exposure to 7.5 μM $Cu^{2+}$. However, all the cells from Clone 9 became spindle-shaped after their exposure to 5 μM $Cu^{2+}$, while all the cells from Clone 19 maintained their elongated shape under the same $Cu^{2+}$ exposure condition. Furthermore, after their exposure to 7.5 μM $Cu^{2+}$, all the cells from Clone 9 turned to a spherical shape, while all the cells from Clone 19 remained unchanged. These clone-to-clone differences were evident in all of the 19 clones I evaluated as shown in Figure 3-9. These results indicate that the morphological features of *E. gracilis* cells are different between their clones under their exposure to $Cu^{2+}$. Since the clone-to-clone differences were most obvious when cells were treated with 7.5 μM $Cu^{2+}$, I decided to use this concentration as an exposure condition for $Cu^{2+}$ removal efficiency measurements as described below.
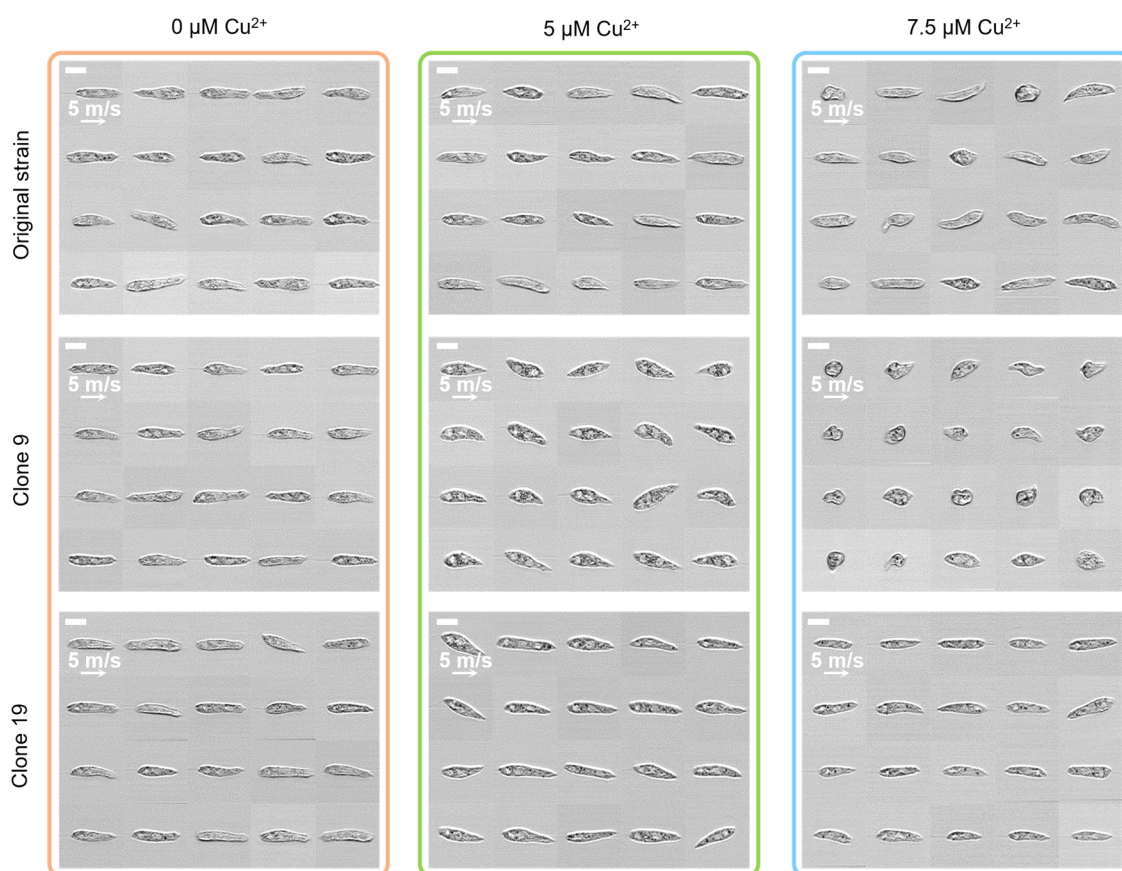
Figure 3-1. Optofluidic time-stretch microscopy images of the original strain, Clone 9, and Clone 19 under different $Cu^{2+}$ stress conditions. These single-cell images were acquired after 2-h $Cu^{2+}$ treatment. Scale bars, 20 μm. See Figure 3-2 for images of all the 19 clones. Reproduced with permission from ref [119]. Copyright 2021 American Chemical Society.

| 0 µM Cu²⁺ | 5 µM Cu²⁺ | 7.5 µM Cu²⁺ |
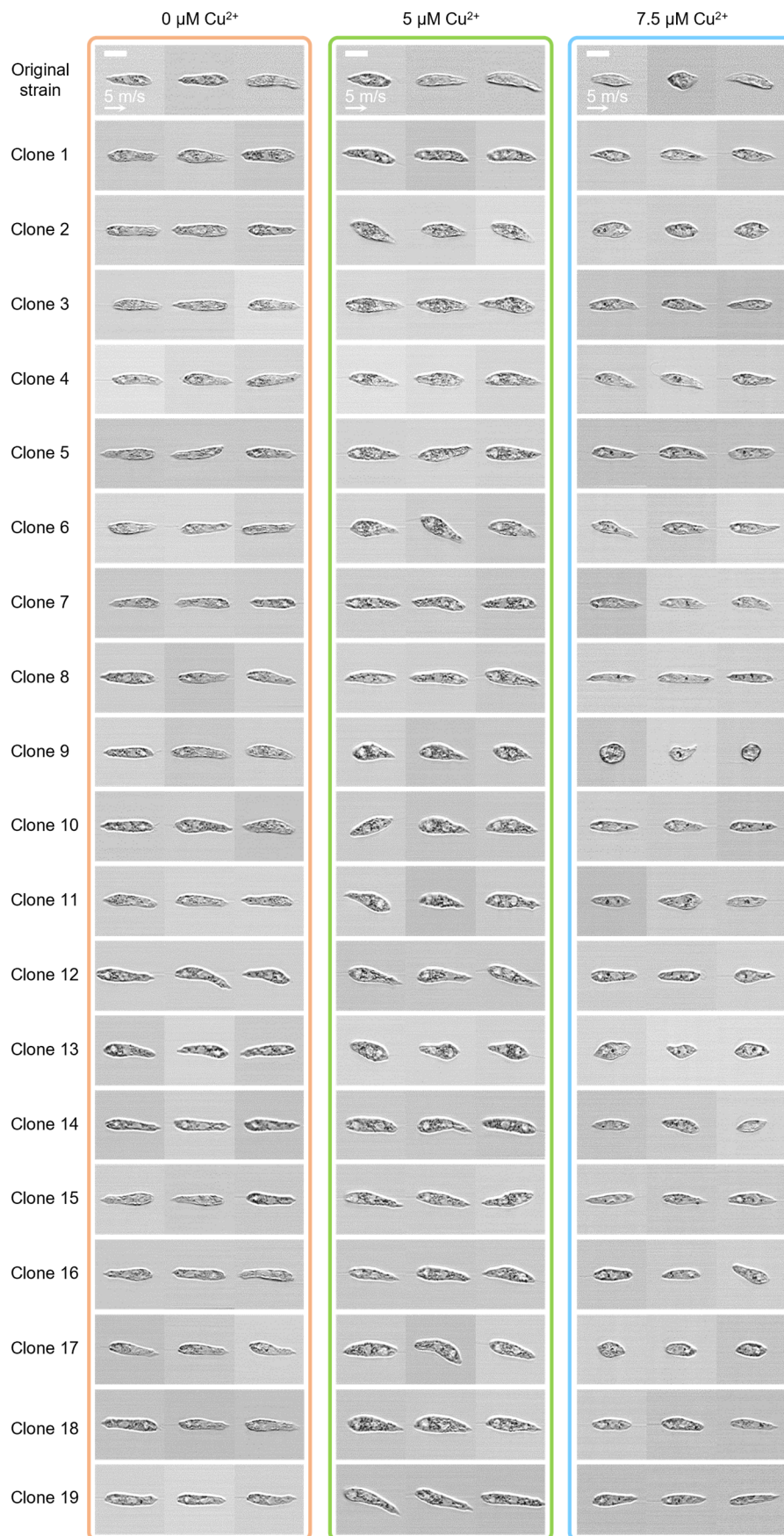
Figure 3-2. Optofluidic time-stretch microscopy images of the original strain and all the 19 *E. gracilis* clones under their exposure for 2 h to different $Cu^{2+}$ concentrations (0 μM, 5 μM, 7.5 μM). Scale bars, 20 μm. N = 144 images per concentration. Reproduced with permission from ref [119]. Copyright 2021 American Chemical Society.

## 3.3 Morphological features of *E. gracilis* clones

To quantitatively investigate, I first extracted the morphological features of *E. gracilis* cells from the acquired images in CellProfiler after segmentation. Specifically, a total of 45 morphological features were extracted from the obtained images. These morphological features were ranked based on their contributions to the cell classification using the SVM. Figure 3-3 shows the top 10 morphological features that made major contributions to the classification. Among them, max Feret diameter (the maximum distance between two parallel lines tangent on either side of the object), major axis length (the length (in pixels) of the major axis of the ellipse that has the same normalized second central moments as the region), min Feret diameter (the minimum distance between two parallel lines tangent on either side of the object), perimeter the total length of the perimeter of the input objects/binary image) and maximum radius (the maximum distance of any pixel in the object to the closest pixel outside of the object) are size-related features obtained from cell images. Eccentricity (the eccentricity of the ellipse that has the same second-moments as the region), compactness (the mean squared distance of the object's pixels from the centroid divided by the area), and form factor [$4\pi \times$(Area)/(Perimeter)$^2$] were calculated in different ways to describe the shape-related features of cells. Zernike features (coefficients to describe a binary object on a basis of Zernike polynomials) characterize the distribution of intensity across each cell. More information on each feature is described in the CellProfiler manual (Measurement, Modules, Manual 3.0), which is available from the following webpage: http://cellprofiler-manual.s3.amazonaws.com/CellProfiler-3.0.0/modules/measurement.html. As shown in Figure 3-3, most of the heavily weighted morphological features were identified to be purely shape- or size-related, without intensity-related information. These results mean that the most significant differences among the 19 clones came from their cell shape and size. More specifically, 10 clones showed the most distinctive difference in eccentricity, compactness, and max Feret diameter. Based on all the extracted morphological features,

a morphological meta-feature that maximized the classification of 19 clones was developed using the LDA.
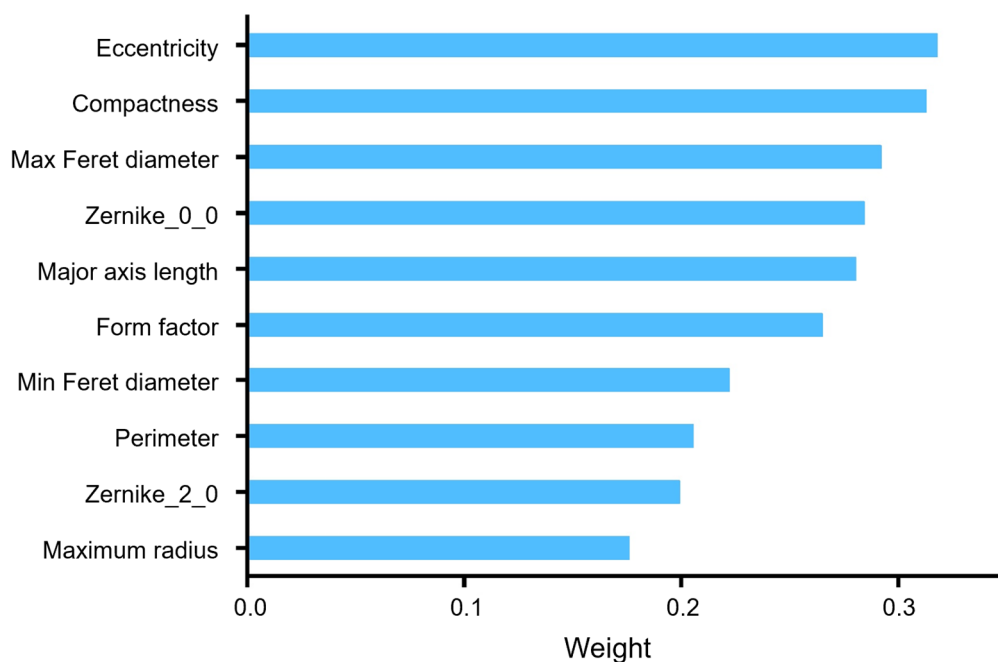


Figure 3-3. Top 10 morphological features of *E. gracilis* cells for classification. Reproduced with permission from ref [119]. Copyright 2021 American Chemical Society.

## 3.4 Cu²⁺ removal efficiency of *E. gracilis* clones

Meanwhile, to evaluate the capability of the 19 clones to remove Cu$^{2+}$, I measured their Cu$^{2+}$ removal efficiency. The results are shown in Table 3-1. The Cu$^{2+}$ removal efficiency varied greatly from clone to clone, ranging from 3.45% to 8.43%. The average Cu$^{2+}$ removal efficiency of the 19 clones was ~5.77%. Because the HM removal efficiency of microalgae varies at different cell concentrations, it is necessary to take the cell concentration into consideration when comparing the Cu$^{2+}$ removal efficiency of the 19 *E. gracilis* clones I measured with reported values. Taking the average cell concentration of $1.04 \times 10^5$ cells/ml 72 h after Cu$^{2+}$ exposure into consideration, the Cu$^{2+}$ removal efficiency per cell concentration was calculated to be ~$5.55 \times 10^{-5}$%/(cells/ml), which is comparable to the concentration value reported previously [~$5.8 \times 10^{-5}$%/(cells/ml)] [64].

Table 3-1. $Cu^{2+}$ removal efficiency of 19 *E. gracilis* clones. Reproduced with permission from ref [119]. Copyright 2021 American Chemical Society.

| Sample | Average removal efficiency (%) N = 3 | Standard deviation (%) |
|---|---|---|
| Clone 1 | 5.93 | 0.19 |
| Clone 2 | 6.53 | 0.44 |
| Clone 3 | 3.94 | 0.68 |
| Clone 4 | 6.20 | 0.30 |
| Clone 5 | 6.15 | 0.88 |
| Clone 6 | 4.76 | 0.43 |
| Clone 7 | 4.49 | 0.41 |
| Clone 8 | 3.45 | 0.12 |
| Clone 9 | 8.43 | 0.75 |
| Clone 10 | 5.82 | 0.23 |
| Clone 11 | 4.80 | 0.34 |
| Clone 12 | 5.91 | 0.40 |
| Clone 13 | 7.82 | 0.57 |
| Clone 14 | 6.91 | 0.35 |
| Clone 15 | 5.95 | 0.43 |
| Clone 16 | 5.17 | 0.65 |
| Clone 17 | 7.57 | 0.33 |
| Clone 18 | 4.88 | 0.57 |
| Clone 19 | 4.94 | 0.44 |

## 3.5 Analysis of the correlation between morphological features and $Cu^{2+}$ removal efficiency

I investigated the potential correlation between the morphology and $Cu^{2+}$ removal efficiency of *E. gracilis* cells using the obtained morphological meta-feature that maximized the classification between the different clones. The scatter plot on the right of Figure 3-4A shows the $Cu^{2+}$ removal efficiencies measured under exposure to 7.5 μM $Cu^{2+}$ against the morphological meta-feature of *E. gracilis* cells under the same condition,

while the left scatter plot shows the $Cu^{2+}$ removal efficiencies measured under exposure to 7.5 µM $Cu^{2+}$ against the morphological meta-feature of cells under exposure to 0 µM $Cu^{2+}$ (i.e., no exposure as a control; see Figure 2-1 for the sample preparation and measurement workflow). Due to the monotonic relation between the two variables (the right scatter plot), I calculated Spearman's rank correlation coefficient ρ to evaluate the correlation between the $Cu^{2+}$ removal efficiency and the morphological meta-feature. The figure shows the presence of a strong monotonic correlation between the $Cu^{2+}$ removal efficiency and meta-feature of *E. gracilis* cells under exposure to 7.5 µM $Cu^{2+}$ (ρ = -0.82 and P = 2.1 × $10^{-5}$). Generally, a ρ value of 0.7 ≤ ρ < 1 or -1 < ρ ≤ -0.7 means strong correlation between two variables. In contrast, this tendency is not shown in the controls (ρ = 0.15 and P = 0.53). These results indicate that the $Cu^{2+}$ exposure was the cause of the morphological alterations seen with the samples exposed to 7.5-µM of $Cu^{2+}$. This conclusion is reinforced by the histogram of the mete-feature of 19 clones under exposure to 0 and 7.5 µM $Cu^{2+}$ (Figure 3-5). Furthermore, the weak correlation between the $Cu^{2+}$ removal efficiency and meta-feature of *E. gracilis* cells under exposure to 0 µM $Cu^{2+}$ means that the meta-feature of cells in the controls could not indicate the $Cu^{2+}$ removal efficiency.

For an intuitive understanding of the meta-feature, single-cell images of each clone with an average meta-feature value are also shown in the scatter plot on the right in Figure 3-4A. The trend of these images indicates that the meta-feature values are highly related to the AR of the cells as the cells with lower AR showed higher $Cu^{2+}$ removal efficiency. This is consistent with the results shown in Figure 3-3. To further investigate this trend, I studied the correlation between the $Cu^{2+}$ removal efficiency and the top 20 morphological features. Specifically, I evaluated these correlations based on Spearman's rank correlation coefficients and P values. As shown in Table 3-2, the top 11 morphological features show stronger monotonic correlations than the others. As expected, 9 of the top 11 morphological features (eccentricity, compactness, max Feret diameter, major axis length, form factor, min Feret diameter, perimeter, maximum radius, and minor axis length) were related to the AR of cells. Among them, I showed the correlation between the $Cu^{2+}$ removal efficiency and the top 3 morphological features (eccentricity, compactness, and max Feret diameter) as representative morphological features. As shown in Figure 3-4B, an increase of $Cu^{2+}$ removal efficiency is strongly correlated with a decrease in

eccentricity ($\rho$ = -0.77, P = 1.3 × 10$^{-4}$), compactness ($\rho$ = -0.81, P = 3.2 × 10$^{-5}$), and max Feret diameter ($\rho$ = -0.75, P = 2.0 × 10$^{-4}$) of *E. gracilis* cells under exposure to 7.5 μM Cu$^{2+}$, but weakly correlated with these top 3 morphological features (eccentricity, $\rho$ = -0.23, P = 0.34; compactness, $\rho$ = -0.16, P = 0.52; max Feret diameter, $\rho$ = 0.12, P = 0.63) of *E. gracilis* cells under exposure to 0 μM Cu$^{2+}$. The values of eccentricity, compactness, and max Feret diameter of *E. gracilis* cells under exposure to 7.5 μM Cu$^{2+}$ were distributed with large variations compared with those the values of *E. gracilis* cells under exposure to 0 μM Cu$^{2+}$, further demonstrating that the Cu$^{2+}$ exposure is the cause of the morphological alterations (see Figures 3-4B, 3-6, 3-7, and 3-8). These results firmly indicate that the morphological features of *E. gracilis* cells under exposure to 7.5 μM Cu$^{2+}$ are reasonable morphological indicators to select *E. gracilis* cells with higher Cu$^{2+}$ removal efficiency.
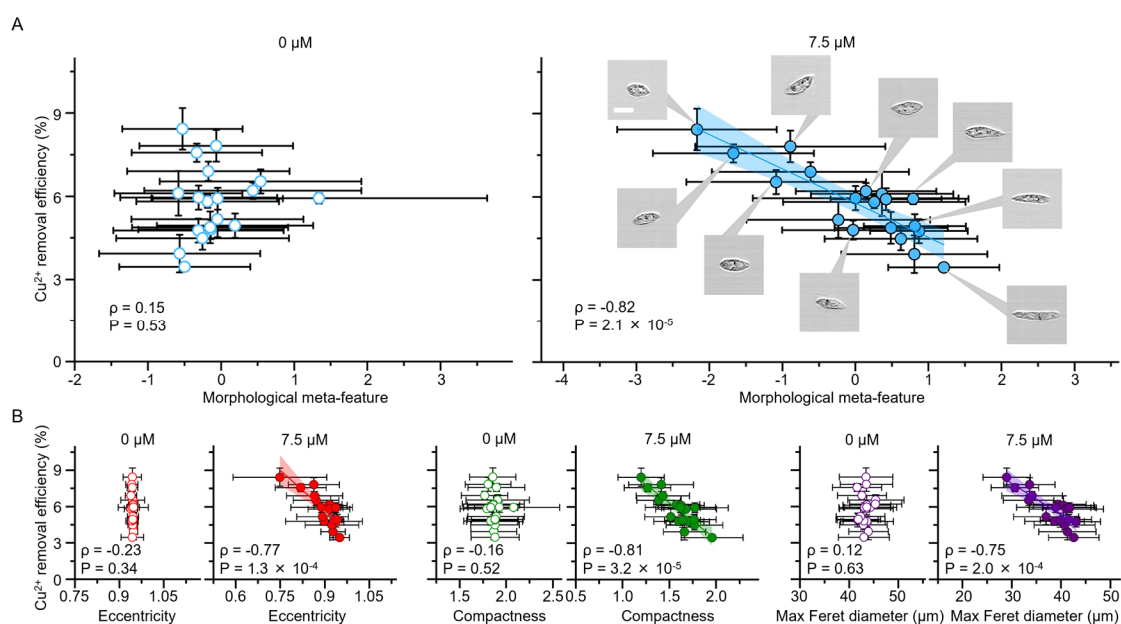
Figure 3-4. Correlation between the morphology and Cu$^{2+}$ removal efficiency of *E. gracilis* cells. (A) Correlation between the morphological meta-feature and Cu$^{2+}$ removal efficiency of *E. gracilis* cells. The meta-feature is a linear combination of 45 morphological features extracted from images of single *E. gracilis* cells exposed to 7.5 μM Cu$^{2+}$ for 2 h, while the Cu$^{2+}$ removal efficiency was measured from the media in which these cells were cultured for 72 h with exposure to 7.5 μM Cu$^{2+}$. (B) Correlation between the top 3 morphological features (eccentricity, compactness, and max Feret diameter) and Cu$^{2+}$ removal efficiency of *E. gracilis* cells. The error bars represent standard deviations of the meta-feature values (n = 144 images) and Cu$^{2+}$ removal efficiency (n = 3 measurements). Scale bar, 20 μm. The colored areas represent 95% confidence intervals. Reproduced with permission from ref [119]. Copyright 2021 American Chemical Society.
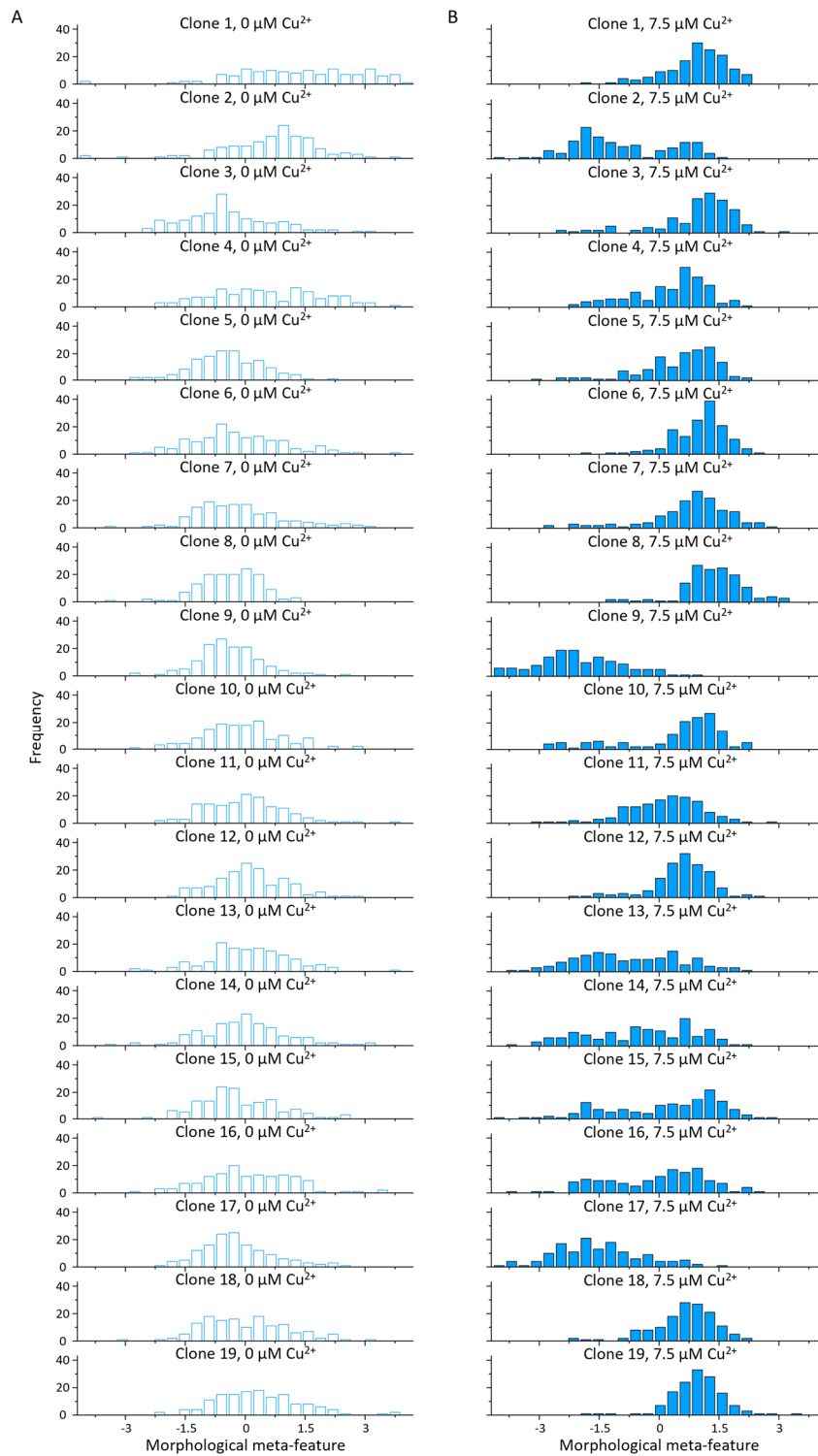
Figure 3-5. Histograms of the morphological meta-feature of *E. gracilis* cells under exposure to (A) 0 and (B) 7.5 μM Cu$^{2+}$. N = 144 images for each clone.
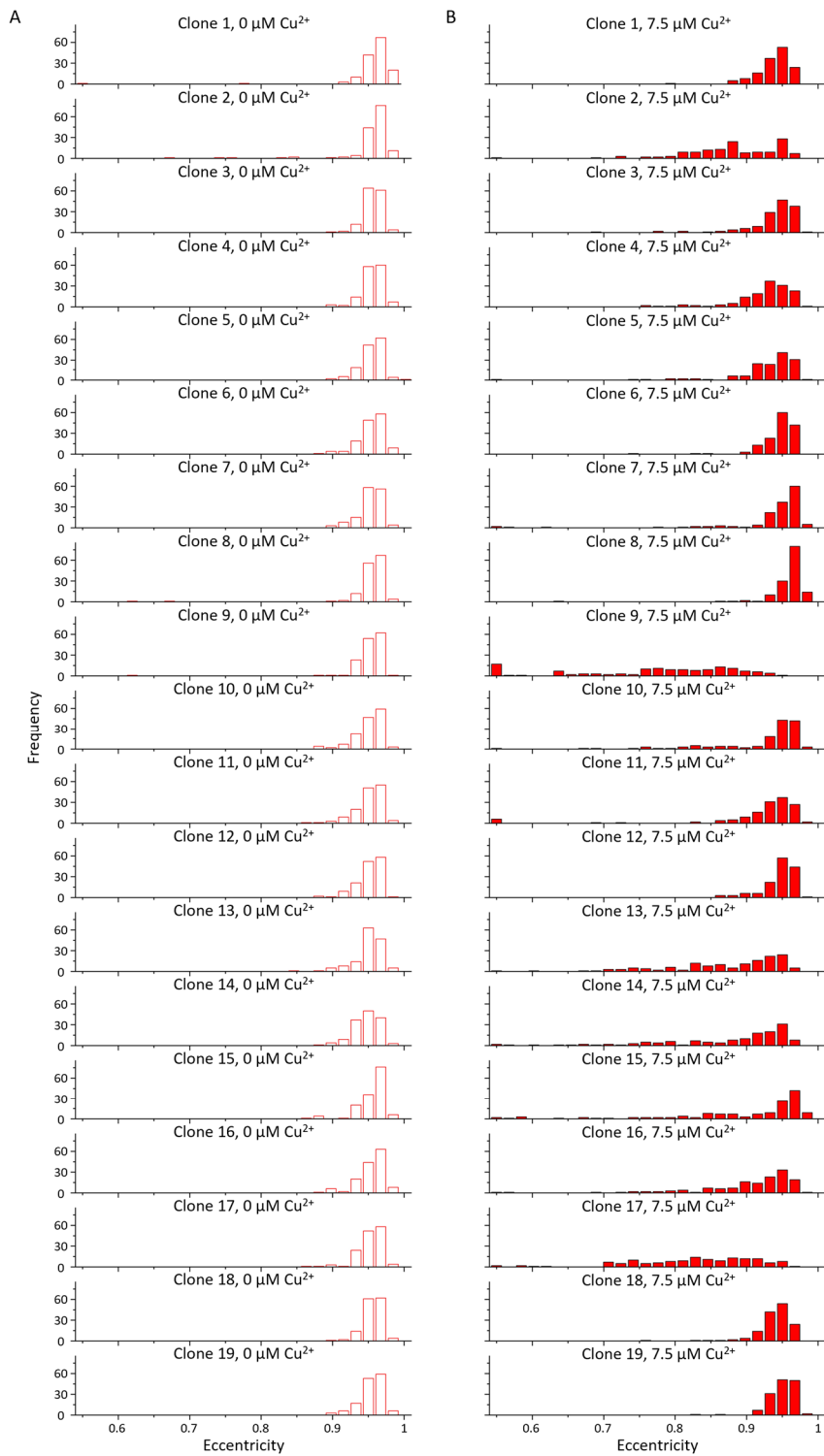
Figure 3-6. Histograms of the eccentricity of *E. gracilis* cells under exposure to (A) 0 and (B) 7.5 μM Cu²⁺.  N = 144 images for each clone.
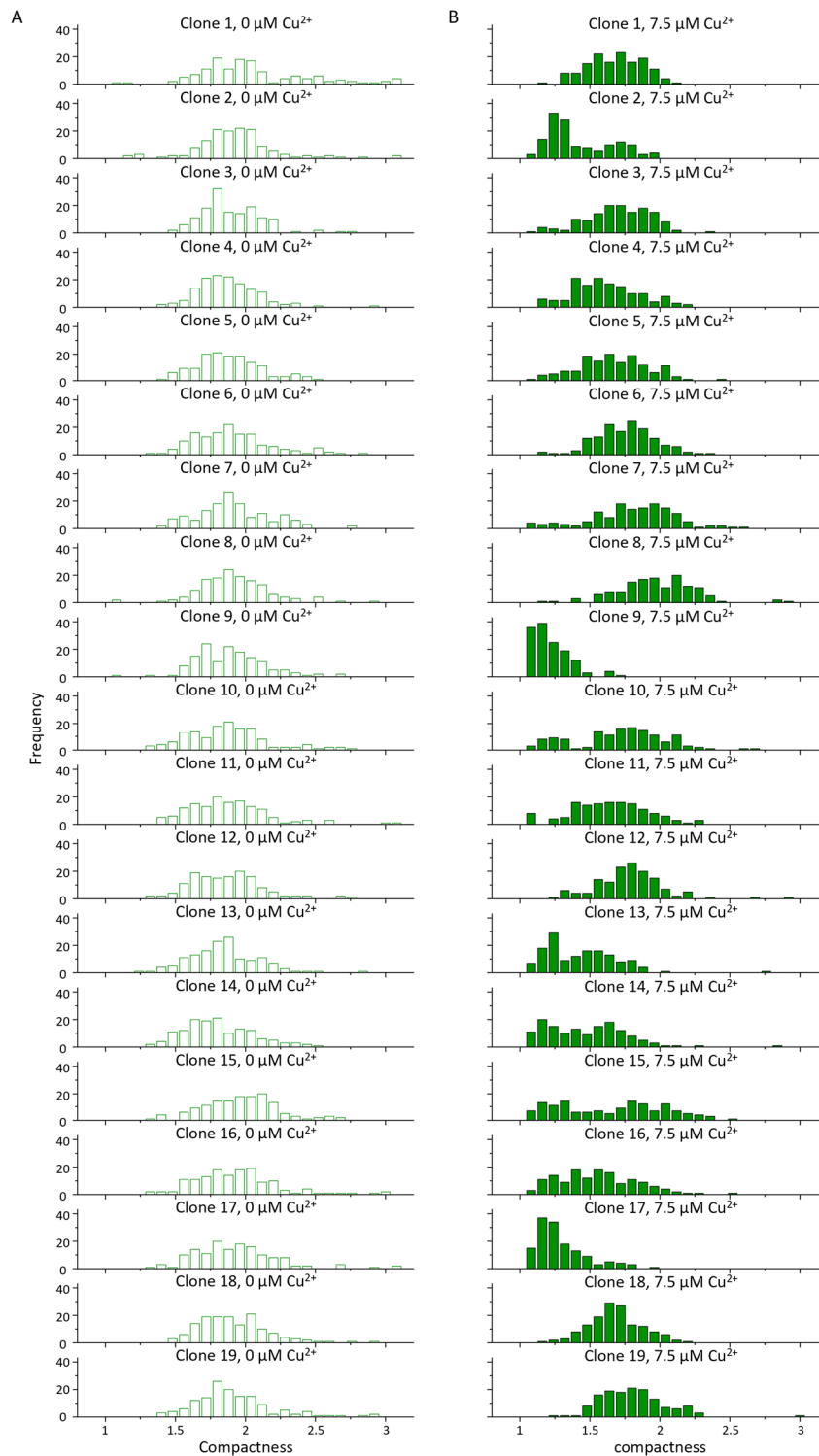
Figure 3-7. Histograms of the compactness of *E. gracilis* cells under exposure to (A) 0 and (B) 7.5 µM Cu²⁺. N = 144 images for each clone.
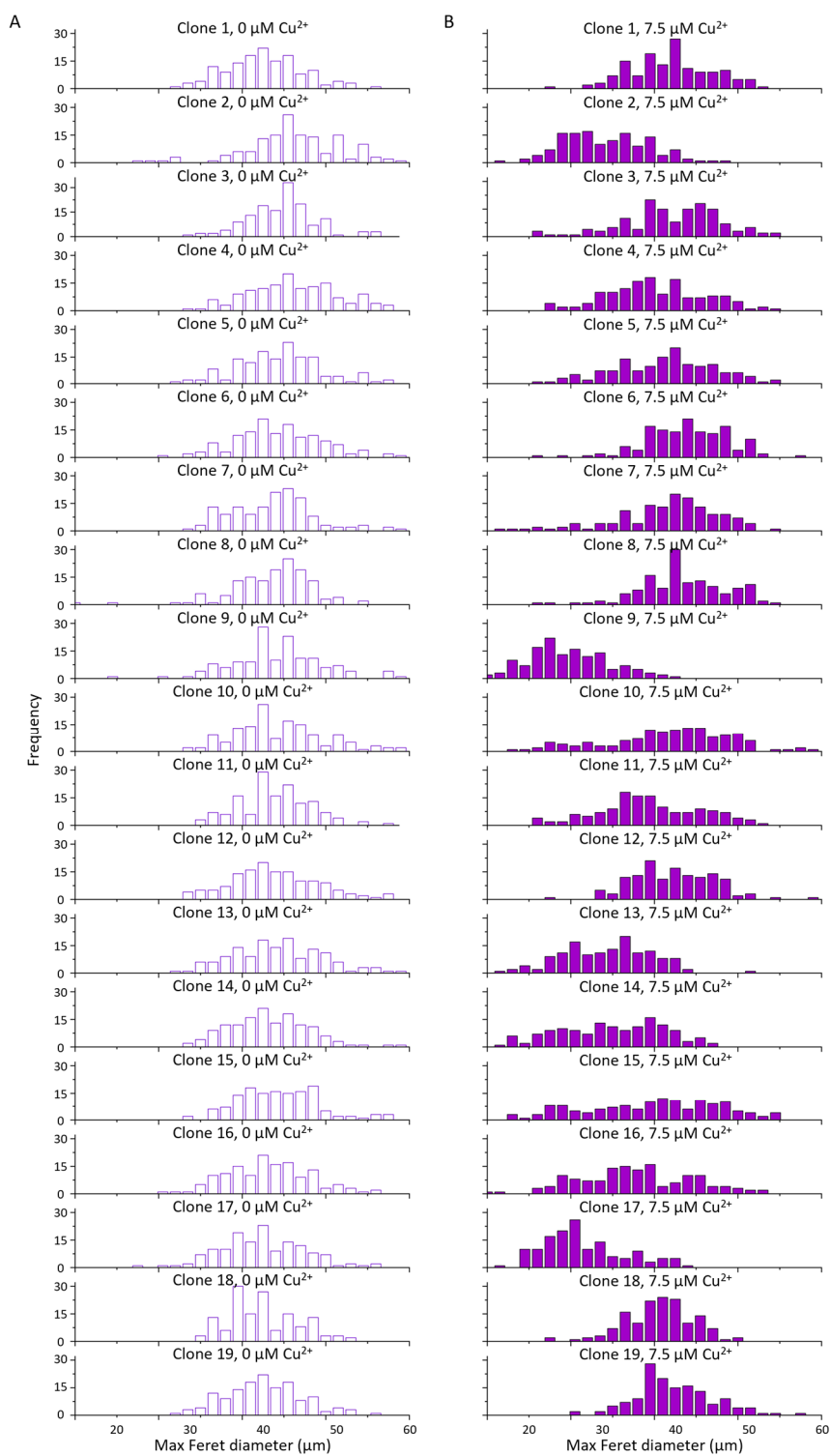
Figure 3-8. Histograms of the max Feret diameter of *E. gracilis* cells under exposure to (A) 0 and (B) 7.5 μM Cu²⁺. N = 144 images for each clone.

Table 3-2. Spearman's rank correlation coefficient and the P value of the top 20 morphological features of *E. gracilis* cells for classification. Reproduced with permission from ref [119]. Copyright 2021 American Chemical Society.

| Morphological feature | Rank | Spearman's rank correlation coefficient ($\rho$) | P value |
|---|---|---|---|
| Eccentricity | 1 | -0.77 | $\leq 0.001$ |
| Compactness | 2 | -0.81 | $\leq 0.0001$ |
| Max Feret diameter | 3 | -0.75 | $\leq 0.001$ |
| Zernike_0_0 | 4 | -0.76 | $\leq 0.001$ |
| Major axis length | 5 | -0.78 | $\leq 0.0001$ |
| Form factor | 6 | 0.77 | $\leq 0.001$ |
| Min Feret diameter | 7 | 0.76 | $\leq 0.001$ |
| Perimeter | 8 | -0.70 | $\leq 0.001$ |
| Zernike_2_0 | 9 | 0.68 | $\leq 0.01$ |
| Maximum radius | 10 | 0.80 | $\leq 0.0001$ |
| Minor axis length | 11 | 0.81 | $\leq 0.0001$ |
| Zernike_4_2 | 12 | -0.60 | $\leq 0.01$ |
| Zernike_6_4 | 13 | -0.64 | $\leq 0.01$ |
| Area | 14 | -0.55 | $\leq 0.05$ |
| Zernike_4_0 | 15 | -0.51 | $\leq 0.05$ |
| Orientation | 16 | -0.24 | $> 0.05$ |
| Zernike_6_6 | 17 | -0.42 | $> 0.05$ |
| Zernike_8_8 | 18 | -0.29 | $> 0.05$ |
| Zernike_2_2 | 19 | 0.22 | $> 0.05$ |
| Mean radius | 20 | 0.61 | $\leq 0.01$ |

## 3.6 Analysis of the growth, viability, and nitrogen consumption

To further understand the cellular activity during $Cu^{2+}$ exposure, I measured the cell growth, viability, and nitrogen consumption of *E. gracilis* cells. As shown in Figure 3-9A, the average growth rate of cells cultured with 7.5 μM $Cu^{2+}$ exposure was ~4 (i.e., cells

divided twice), which is comparable to the estimated growth of cells cultured without $Cu^{2+}$ exposure (see Figure 3-10 for the growth of *E. gracilis* cells from the original strain without $Cu^{2+}$ exposure). Figure 2-6 shows the detailed cell growth of 19 clones on each day. The cells grew constantly from the time of exposure to 7.5 μM $Cu^{2+}$ (day 22) to 48 h after the exposure (day 24) because the cells were in the logarithmic phase, though the growth almost saturated 48 h after the exposure. Furthermore, as shown in Figure 3-9B and Figure 2-6, the cell viability was close to 100% before and during the $Cu^{2+}$ exposure. These results indicate that the proliferative activity of *E. gracilis* cells during 7.5 μM $Cu^{2+}$ exposure for 72 h was not suppressed from the stress of $Cu^{2+}$. In addition, as shown in all the panels of Figure 3-9, the correlations between the $Cu^{2+}$ removal efficiency of *E. gracilis* cells and their growth, viability, and nitrogen consumption were weak and statistically insignificant (cell growth: $\rho = -0.31$, $P = 0.20$; cell viability: $\rho = -0.10$, $P = 0.27$; nitrogen consumption: $\rho = -0.14$, $P = 0.58$). These results indicate that the $Cu^{2+}$ removal efficiency differences between clones were not caused by the variations of the cell growth, viability, or nitrogen consumption.
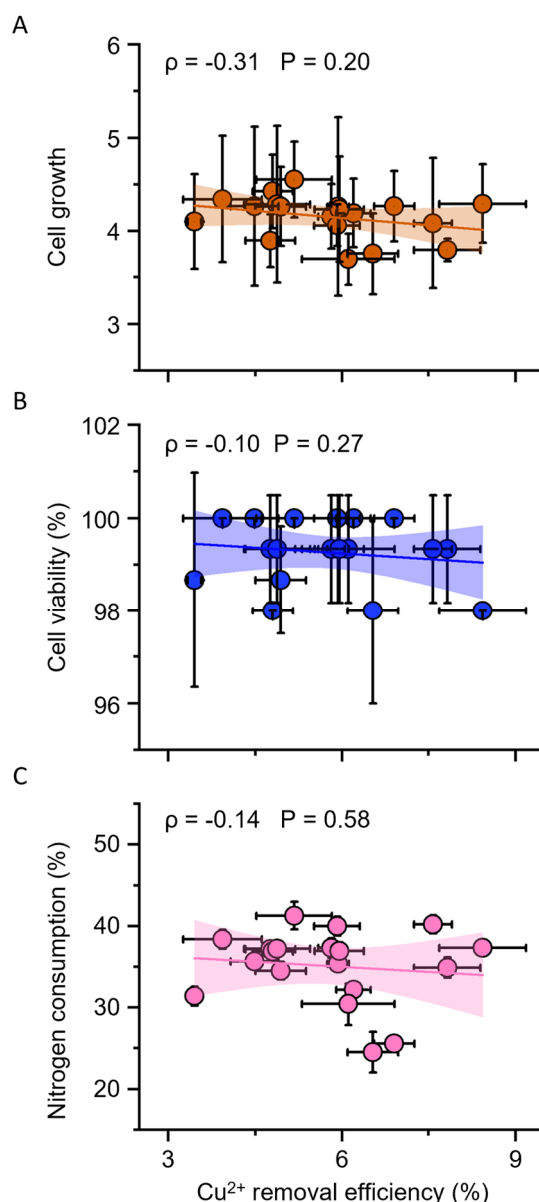
Figure 3-9. Correlations between the $Cu^{2+}$ removal efficiency and the growth, viability, and nitrogen consumption of *E. gracilis* cells. (A) Correlation between the $Cu^{2+}$ removal efficiency and cell growth during $Cu^{2+}$ exposure. The cell growth was calculated as the number of cells 72 h after $Cu^{2+}$ exposure divided by the number of cells before $Cu^{2+}$ exposure. (B) Correlation between the $Cu^{2+}$ removal efficiency and cell viability 72 h after $Cu^{2+}$ exposure. (C) Correlation between the $Cu^{2+}$ removal efficiency and nitrogen consumption of *E. gracilis* cells. The nitrogen consumptions were calculated as the difference of the total nitrogen concentrations (nitrate-nitrogen and ammonium-nitrogen) before and 72 h after $Cu^{2+}$ exposure divided by the sum of the total nitrogen concentrations before the exposure. The error bars represent standard deviations of cell concentrations (n = 3 measurements). The colored areas represent 95% confidence intervals. Reproduced with permission from ref [119]. Copyright 2021 American Chemical Society with minor modifications.
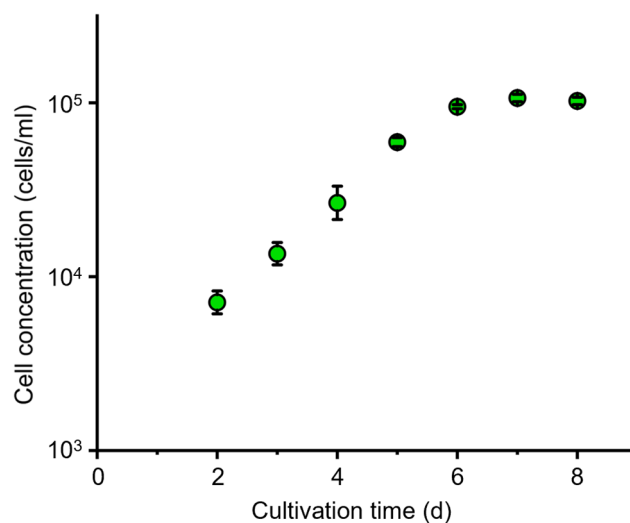
Figure 3-10. Cell concentration of the original strain of *E. gracilis* during culturing in AF-6 medium. The error bars represent standard deviations of cell concentrations (n = 3 measurements). Reproduced with permission from ref [119]. Copyright 2021 American Chemical Society.

## 3.7 Summary

In this chapter, I demonstrated an intelligent morphological indicator of microalgal HM removal efficiency that can be used for directed evolution of microalgae, which has great potential for the development of *E. gracilis* with an extremely high HM removal efficiency for practical wastewater treatment worldwide. First, I successfully obtained 19 clones derived from single *E. gracilis* cells and cultured them in the synchronized life cycle and culture conditions. Second, I obtained single-cell images of the 19 clones under different $Cu^{2+}$ exposure conditions and analyzed their morphological features using machine learning. The morphological features differed the most among clones with exposure to 7.5 µM $Cu^{2+}$. Meanwhile, I measured the $Cu^{2+}$ removal efficiency of the 19 clones. Finally, the morphological indicator of microalgal HM removal efficiency was confirmed by a strong monotonic correlation (Spearman's $\rho = -0.82$, $P = 2.1 \times 10^{-5}$) between a morphological meta-feature recognized via the machine learning algorithms and the $Cu^{2+}$ removal efficiency of 19 *E. gracilis* clones. Further analysis indicated that the $Cu^{2+}$ removal efficiency differences between clones were not caused by the variations of the cell growth, viability, or nitrogen consumption.

# Chapter 4

# Conclusions

In this thesis, I proposed and experimentally demonstrated an intelligent morphological indicator. This morphological indicator is critical to the realization of non-invasive and label-free sorting of *E. gracilis* cells with high $Cu^{2+}$ removal efficiency, thus enabling the development of *E. gracilis* with an extremely high HM removal efficiency for practical wastewater treatment based on directed evolution. Specifically, I successfully prepared clones derived from single *E. gracilis* cells, which showed heterogeneity in both morphological response to $Cu^{2+}$ and $Cu^{2+}$ removal efficiency. To keep the clone samples in well-controlled conditions, I prepared and treated the single cell-derived clones in the same culture conditions. Analysis of a morphological meta-feature under exposure to 7.5 $\mu M$ $Cu^{2+}$ recognized via our machine learning algorithms and the $Cu^{2+}$ removal efficiency of 19 *E. gracilis* clones showed a strong monotonic correlation (Spearman's $\rho = -0.82$, P $= 2.1 \times 10^{-5}$) between them. In comparison, there was only a weak correlation (Spearman's $\rho = 0.15$, P $= 0.53$) between the morphological meta-feature under exposure to 0 $\mu M$ $Cu^{2+}$ recognized in the same way and the $Cu^{2+}$ removal efficiency of 19 *E. gracilis* clones. Similar results were shown in the top 3 morphological features. These results suggest that the morphological features could be effective indicators of microalgal HM removal efficiency.

The morphological indicator of *E. gracilis* identified in this work has the potential for enabling directed-evolution-based development of *E. gracilis* with high $Cu^{2+}$ removal efficiency. Specifically, this can be achieved by physically isolating *E. gracilis* cells with much higher $Cu^{2+}$ removal efficiency than the average by implementing the indicator information on recently developed powerful sorting techniques, such as inertial-microfluidics-based sorting [130, 131] and image-activated cell sorting [99-104]. Inertial-microfluidics-based sorting can be used to separate *E. gracilis* cells based on cellular AR [130], which is analogous to cellular eccentricity, as shown in Figure 3-7B. The throughput of this sorting technique was demonstrated to be ~1300 cells/s using a previously developed sorter by Li et al [130]. Intelligent image-activated cell sorting can

be employed to sort *E. gracilis* cells based on a combination of various morphological features, such as the morphological meta-feature, as shown in Figure 3-7A, by simply modifying algorithms used for the decision making of sorting on the real-time intelligent image processor [99-104]. The second generation of the intelligent image-activated cell sorting technique is now available to sort cells with a high throughput of ~2000 cells/s [100].

After solving the challenges in the cell sorting step, to demonstrate the whole process of directed evolution of microalgae with high HM removal efficiency, it is necessary to overcome the scientific and practical bottlenecks in the mutagenesis step of the directed-evolution process. A suitable mutagenesis method and conditions are highly dependent on species and purpose. There are few reports about mutagenesis on the nuclear genome of *E. gracilis* as it is a polyploid [132]. Our group previously reported a mutagenesis method, Fe-ion beam irradiation, on *E. gracilis* for obtaining oil-rich cells through directed evolution [133], but further analysis is necessary to check if this method is applicable to the purpose of this thesis. In addition, the accessibility of Fe-ion beam irradiation is very limited, which is a practical problem for carrying out multiple rounds of directed evolution. Other methods of mutagenesis, such as atmosphere room-temperature plasma (ARTP), are worth trying. ARTP has been successfully used on *Crypthecodinium cohnii* for breeding extracellular polysaccharide-rich cells [134] and *Chlorella pyrenoidosa* [135] for screening an optimal mutant strain with increased lipid productivity. But the applicability of this method on *E. gracilis* for obtaining cells with a high HM removal efficiency remains to be investigated.

In conclusion, I proposed and experimentally demonstrated an intelligent morphological indicator of the $Cu^{2+}$ removal efficiency of *E. gracilis*. This intelligent morphological indicator is crucial for the development of a directed-evolution method of microalgae with high HM removal efficiency, because it is the first found non-invasive and label-free indicator that can be used to sort microalgal cells with high HM removal efficiency. Using the same methods, it is highly possible to experimentally demonstrate more morphological indicators of other HMs' removal efficiency of *E. gracilis* and other types of microalgal species, as long as these microalgal species also show differences in morphological response and removal efficiency after HM exposure among cells. This indicator can be implemented on the powerful single-cell sorting techniques [99-104, 130,

131] to achieve a fast and accurate sorting of microalgal cells with high HM removal efficiency. To demonstrate the whole process of directed evolution of microalgae with high HM removal efficiency, a suitable mutagenesis method and conditions are also necessary but presently remains unsolved. However, there are several promising candidates that are worth trying. Overall, the morphological indicator of microalgal HM removal efficiency I demonstrated in this thesis has the great potential for directed-evolution-based development of microalgae with extremely high HM removal efficiency, thus benefit to a not only sustainable, low-cost, and eco-friendly, but also highly efficient bioremediation method for the treatment of HM-polluted wastewater.

# Table of Acronyms

| Acronyms | Full Name |
| --- | --- |
| HM | heavy metal |
| AR | aspect ratio |
| MTs | metallothioneins |
| MTLPs | metallothionein-like proteins |
| PCs | phytochelatins |
| SVM | support vector machine |
| LDA | linear discriminant analysis |
| FACS | fluorescence-activated cell sorting |
| ICP-AES | inductively coupled plasma atomic emission spectrometry |
| ARTP | atmosphere room-temperature plasma |

# Publications

During my Ph.D., I have worked on projects that are mainly related to the morphological indicator of microalgal HM removal efficiency. Listed below are my publication in peer-reviewed journals.

Publication related to this thesis:

1. Xu, M.; Harmon, J.; Yuan, D.; Yan, S.; Lei, C.; Hiramatsu, K.; Zhou, Y.; Loo, M. H.; Hasunuma, T.; Isozaki, A.; Goda, K., "Morphological Indicator for Directed Evolution of *Euglena gracilis* with a High Heavy Metal Removal Efficiency," *Environmental Science & Technology*, **2021**, 55, 7880.

2. Isozaki, A.; Mikami, H.; Tezuka, H.; Matsumura, H.; Huang, K.; Akamine, M.; Hiramatsu, K.; Iino, T.; Ito, T.; Karakawa, H.; Kasai, Y.; Li, Y.; Nakagawa, Y.; Ohnuki, S.; Ota, T.; Qian, Y.; Sakuma, S.; Sekiya, T.; Shirasaki, Y. Y.; Suzuki, N.; Tayyabi, E.; Wakamiya, T.; Xu, M.; Yamagishi, M.; Yan, H.; Yu, Q.; Yan, S.; Yuan, D.; Zhang, W.; Zhao, Y.; Arai, F.; Campbell, R. E.; Danelon, C.; Di Carlo, D.; Hiraki, K.; Hoshino, Y.; Hosokawa, Y.; Inaba, M.; Nakagawa, A.; Ohya, Y.; Oikawa, M.; Uemura, S.; Ozeki, Y.; Sugimura, T.; Nitta, N.; Goda, K., "Intelligent Image-Activated Cell Sorting 2.0," *Lab on a Chip*, **2020**, 20, 2263.

3. Yan, H.; Wu, Y.; Zhou, Y.; Xu, M.; Paiè, P.; Lei, C.; Yan, S.; Goda, K., "Virtual Optofluidic Time-Stretch Quantitative Phase Imaging," *APL Photonics*, **2020**, 5, 046103.

# Bibliography

[1]     A. H. Smith, E. O. Lingas and M. Rahman. Contamination of drinking-water by arsenic in Bangladesh: a public health emergency. Bulletin of the World Health Organization 78, 1093-1103 (2000).

[2]     R. F. Butterworth. Metal toxicity, liver disease and neurodegeneration. Neurotoxicity Research 18, 100-105 (2010).

[3]     K. Manna, B. Debnath and W. Singh. Sources and toxicological effects of lead on human health. Indian Journal of Medical Specialities 10, 66-71 (2019).

[4]     Z. Visnjic-Jeftic, I. Jaric, L. Jovanovic, S. Skoric, M. Smederevac-Lalic, M. Nikcevic and M. Lenhardt. Heavy metal and trace element accumulation in muscle, liver and gills of the Pontic shad (*Alosa immaculata* Bennet 1835) from the Danube River (Serbia). Microchemical Journal 95, 341-344 (2010).

[5]     G. Gobe and D. Crane. Mitochondria, reactive oxygen species and cadmium toxicity in the kidney. Toxicology Letters 198, 49-55 (2010).

[6]     L. Bucio, C. García, V. Souza, E. Hernández, C. González, M. Betancourt and M. C. Gutiérrez-Ruiz. Uptake, cellular distribution and DNA damage produced by mercuric chloride in a human fetal hepatic cell line. Mutation Research/Fundamental and Molecular Mechanisms of Mutagenesis 423, 65-72 (1999).

[7]     Z. X. Wang, J. Q. Chen, L. Y. Chai, Z. H. Yang, S. H. Huang and Y. Zheng. Environmental impact and site-specific human health risks of chromium in the vicinity of a ferro-alloy manufactory, China. Journal of Hazardous Materials 190, 980-985 (2011).

[8]     L. M. Camacho, M. Gutierrez, M. T. Alarcon-Herrera, L. Villalba Mde and S. Deng. Occurrence and treatment of arsenic in groundwater and soil in northern Mexico and southwestern USA. Chemosphere 83, 211-225 (2011).

[9]     A. Duda-Chodak and U. Blaszczyk. The impact of nickel on human health. Journal of Elementology 13, 685-693 (2008).

[10]    M. F. Bouchard, S. Sauve, B. Barbeau, M. Legrand, M. E. Brodeur, T. Bouffard, E. Limoges, D. C. Bellinger and D. Mergler. Intellectual impairment in school-age children exposed to manganese from drinking water. Environmental Health Perspectives 119, 138-143 (2011).

[11]    T. A. Kurniawan, G. Y. S. Chan, W.-H. Lo and S. Babel. Physico–chemical treatment techniques for wastewater laden with heavy metals. Chemical Engineering Journal 118, 83-98 (2006).

[12]    B. E. Igiri, S. I. R. Okoduwa, G. O. Idoko, E. P. Akabuogu, A. O. Adeyi and I. K. Ejiogu. Toxicity and bioremediation of heavy metals contaminated ecosystem from tannery wastewater: a review. International Journal of Toxicology 2018, 2568038 (2018).

[13] K. Yin, Q. Wang, M. Lv and L. Chen. Microorganism remediation strategies towards heavy metals. Chemical Engineering Journal 360, 1553-1563 (2019).

[14] L. K. Wang, D. A. Vaccari, Y. Li and N. K. Shammas, Chemical precipitation, in: L. K. Wang, Y. T. Hung and N. K. Shammas (Eds.) Physicochemical treatment processes, Humana Press, 2005, pp. 141-197.

[15] M. A. Keane. The removal of copper and nickel from aqueous solution using Y zeolite ion exchangers. Colloids and Surfaces A: Physicochemical and Engineering Aspects 138, 11-20 (1998).

[16] A. Lalmi, K.-E. Bouhidel, B. Sahraoui and C. e. H. Anfif. Removal of lead from polluted waters using ion exchange resin with $Ca(NO_3)_2$ for elution. Hydrometallurgy 178, 287-293 (2018).

[17] A. Aliane, N. Bounatiro, A. T. Cherif and D. E. Akretche. Removal of chromium from aqueous solution by complexation – ultrafiltration using a water-soluble macroligand. Water Research 35, 2320-2326 (2001).

[18] A. Wahab Mohammad, R. Othaman and N. Hilal. Potential use of nanofiltration membranes in treatment of industrial wastewater from Ni-P electroless plating. Desalination 168, 241-252 (2004).

[19] N. Abdullah, N. Yusof, W. J. Lau, J. Jaafar and A. F. Ismail. Recent trends of heavy metal removal from water/wastewater by membrane technologies. Journal of Industrial and Engineering Chemistry 76, 17-38 (2019).

[20] D. Zamboulis, S. I. Pataroudi, A. I. Zouboulis and K. A. Matis. The application of sorptive flotation for the removal of metal ions. Desalination 162, 159-168 (2004).

[21] L. Chang, Y. Cao, G. Fan, C. Li and W. Peng. A review of the applications of ion floatation: wastewater treatment, mineral beneficiation and hydrometallurgy. RSC Advances 9, 20226-20239 (2019).

[22] L. Semerjian and G. M. Ayoub. High-pH–magnesium coagulation–flocculation in wastewater treatment. Advances in Environmental Research 7, 389-403 (2003).

[23] C. Y. Teh, P. M. Budiman, K. P. Y. Shak and T. Y. Wu. Recent advancement of coagulation–flocculation and its application in wastewater treatment. Industrial & Engineering Chemistry Research 55, 4363-4389 (2016).

[24] T. Subbaiah, S. C. Mallick, K. G. Mishra, K. Sanjay and R. P. Das. Electrochemical precipitation of nickel hydroxide. Journal of Power Sources 112, 562-569 (2002).

[25] M. Tedesco, H. V. M. Hamelers and P. M. Biesheuvel. Nernst-Planck transport theory for (reverse) electrodialysis: I. Effect of co-ion transport through the membranes. Journal of Membrane Science 510, 370-381 (2016).

[26] S. Rezania, S. M. Taib, M. F. Md Din, F. A. Dahalan and H. Kamyab. Comprehensive review on phytotechnology: Heavy metals removal by diverse aquatic plants species from wastewater. Journal Hazardous Materials 318, 587-599 (2016).

[27] Y. Du, Q. Wu, D. Kong, Y. Shi, X. Huang, D. Luo, Z. Chen, T. Xiao and J. Y. S. Leung. Accumulation and translocation of heavy metals in water hyacinth:

Maximising the use of green resources to remediate sites impacted by e-waste recycling activities. Ecological Indicators 115, 106384 (2020).

[28]  P. A. Brown, S. A. Gill and S. J. Allen. Metal removal from wastewater using peat. Water Research 34, 3907-3916 (2000).

[29]  J. De, N. Ramaiah and L. Vardanyan. Detoxification of toxic heavy metals by marine bacteria highly resistant to mercury. Marine Biotechnology 10, 471-477 (2008).

[30]  M. Ahemad. Remediation of metalliferous soils through the heavy metal resistant plant growth promoting bacteria: Paradigms and prospects. Arabian Journal of Chemistry 12, 1365-1377 (2019).

[31]  F. Yong-Qian. Biosorption of copper (II) from aqueous solution by mycelial pellets of *Rhizopus oryzae*. African Journal of Biotechnology 11, 1403-1411 (2012).

[32]  Q. Li, J. Liu and G. M. Gadd. Fungal bioremediation of soil co-contaminated with petroleum hydrocarbons and toxic metals. Applied Microbiology and Biotechnology 104, 8999-9008 (2020).

[33]  A. K. Zeraatkar, H. Ahmadzadeh, A. F. Talebi, N. R. Moheimani and M. P. McHenry. Potential use of algae for heavy metal bioremediation, a critical review. Journal of Environmental Management 181, 817-831 (2016).

[34]  K. Suresh Kumar, H. U. Dahms, E. J. Won, J. S. Lee and K. H. Shin. Microalgae - A promising tool for heavy metal remediation. Ecotoxicology and Environmental Safety 113, 329-352 (2015).

[35]  R. Chaney, Plant uptake of inorganic waste constitutes, in: J. Parr, P. Marsh and J. Kla (Eds.) Land treatment of hazardous wastes, Noyes Data Corporation, Park Ridge, NJ, 1983, pp. 50-76.

[36]  N. Aurangzeb, S. Nisa, Y. Bibi, F. Javed and F. Hussain. Phytoremediation potential of aquatic herbs from steel foundry effluent. Brazilian Journal of Chemical Engineering 31, 881-886 (2014).

[37]  B. Dhir, P. Sharmila, P. Pardha Saradhi and S. A. Nasim. Physiological and antioxidant responses of *Salvinia natans* exposed to chromium-rich wastewater. Ecotoxicology and Environmental Safety 72, 1790-1797 (2009).

[38]  Q. Lu, Z. L. He, D. A. Graetz, P. J. Stoffella and X. Yang. Uptake and distribution of metals by water lettuce (*Pistia stratiotes* L.). Environmental Science and Pollution Research 18, 978-986 (2011).

[39]  W. A. Glooschenko and J. A. Capobianco. Trace element content of northern Ontario peat. Environmental Science & Technology 16, 187-188 (1982).

[40]  P. Pakarinen, K. Tolonen, S. Heikkinen and A. Nurmi. Accumulation of metals in finnish raised bogs. Ecological Bulletins 35, 377-382 (1983).

[41]  R. H. Crist, J. R. Martin, J. Chonko and D. R. Crist. Uptake of metals on peat moss: an ion-exchange process. Environmental Science & Technology 30, 2456-2461 (1996).

[42]  G. P. Sheng, J. Xu, H. W. Luo, W. W. Li, W. H. Li, H. Q. Yu, Z. Xie, S. Q. Wei

and F. C. Hu. Thermodynamic analysis on the binding of heavy metals onto extracellular polymeric substances (EPS) of activated sludge. Water Research 47, 607-614 (2013).

[43]    T. S. Anirudhan, S. Jalajamony and S. S. Sreekumari. Adsorption of heavy metal ions from aqueous solutions by amine and carboxylate functionalised bentonites. Applied Clay Science 65-66, 67-71 (2012).

[44]    S. Dave, M. Damani and D. Tipre. Copper remediation by *Eichhornia* spp. and sulphate-reducing bacteria. Journal of Hazardous Materials 173, 231-235 (2010).

[45]    F. Huang, Z. Dang, C.-L. Guo, G.-N. Lu, R. R. Gu, H.-J. Liu and H. Zhang. Biosorption of Cd(II) by live and dead cells of *Bacillus cereus* RC-1 isolated from cadmium-contaminated soil. Colloids and Surfaces B: Biointerfaces 107, 11-18 (2013).

[46]    E. Khadivinia, H. Sharafi, F. Hadi, H. S. Zahiri, S. Modiri, A. Tohidi, A. Mousavi, A. H. Salmanian and K. A. Noghabi. Cadmium biosorption by a glyphosate-degrading bacterium, a novel biosorbent isolated from pesticide-contaminated agricultural soils. Journal of Industrial and Engineering Chemistry 20, 4304-4310 (2014).

[47]    T. Limcharoensuk, N. Sooksawat, A. Sumarnrote, T. Awutpet, M. Kruatrachue, P. Pokethitiyook and C. Auesukaree. Bioaccumulation and biosorption of $Cd^{2+}$ and $Zn^{2+}$ by bacteria isolated from a zinc mine in Thailand. Ecotoxicology and Environmental Safety 122, 322-330 (2015).

[48]    J. E. Duddridge and M. Wainwright. Heavy metal accumulation by aquatic fungi and reduction in viability of *Gammarus pulex* fed $Cd^{2+}$ contaminated mycelium. Water Research 14, 1605-1611 (1980).

[49]    M. Shakya, P. Sharma, S. S. Meryem, Q. Mahmood and A. Kumar. Heavy metal removal from industrial wastewater using fungi: uptake mechanism and biochemical aspects. Journal of Environmental Engineering 142, C6015001 (2016).

[50]    S. Amirnia, M. B. Ray and A. Margaritis. Heavy metals removal from aqueous solutions using *Saccharomyces cerevisiae* in a novel continuous bioreactor–biosorption system. Chemical Engineering Journal 264, 863-872 (2015).

[51]    E. Bazrafshan, A. A. Zarei and F. K. Mostafapour. Biosorption of cadmium from aqueous solutions by *Trichoderma* fungus: kinetic, thermodynamic, and equilibrium study. Desalination and Water Treatment 57, 14598-14608 (2016).

[52]    B. Dhal, Abhilash and B. D. Pandey. Mechanism elucidation and adsorbent characterization for removal of Cr(VI) by native fungal adsorbent. Sustainable Environment Research 28, 289-297 (2018).

[53]    S. Iram and S. Abrar. Biosorption of copper and lead by heavy metal resistant fungal isolates. International Journal of Scientific and Research Publications 5, 1-5 (2015).

[54]    L. Ramrakhiani, R. Majumder and S. Khowala. Removal of hexavalent chromium by heat inactivated fungal biomass of *Termitomyces clypeatus*: Surface

characterization and mechanism of biosorption. Chemical Engineering Journal 171, 1060-1068 (2011).

[55]    S. K. Mehta and J. P. Gaur. Use of algae for removing heavy metal ions from wastewater: progress and prospects. Critical Reviews in Biotechnology 25, 113-152 (2005).

[56]    S. Y. Cheng, P. L. Show, B. F. Lau, J. S. Chang and T. C. Ling. New prospects for modified algae in heavy metal adsorption. Trends in Biotechnology 37, 1255-1268 (2019).

[57]    I. Priyadarshani, D. Sahu and B. Rath. Microalgal bioremediation: current practices and perspectives. Journal of Biochemical Technology 3, 299-304 (2011).

[58]    B. Volesky and Z. Holan. Biosorption of heavy metals. Biotechnology Progress 11, 235-250 (1995).

[59]    R. H. Whittater, Communities and Ecosystems, 2 ed., MacMillan, New York, 1975.

[60]    C. E. Blaby-Haas and S. S. Merchant. The ins and outs of algal metal transport. Biochimica et Biophysica Acta (BBA) - Molecular Cell Research 1823, 1531-1552 (2012).

[61]    H. V. Perales-Vela, J. M. Peña-Castro and R. O. Cañizares-Villanueva. Heavy metal detoxification in eukaryotic microalgae. Chemosphere 64, 1-10 (2006).

[62]    C.-J. Tien, D. C. Sigee and K. N. White. Copper adsorption kinetics of cultured algal cells and freshwater phytoplankton with emphasis on cell surface characteristics. Journal of Applied Phycology 17, 379-389 (2005).

[63]    H. Yan and G. Pan. Toxicity and bioaccumulation of copper in three green microalgal species. Chemosphere 49, 471-476 (2002).

[64]    C. Winters, C. Guéguen and A. Noble. Equilibrium and kinetic studies of Cu(II) and Ni(II) sorption on living *Euglena gracilis*. Journal of Applied Phycology 29, 1391-1398 (2016).

[65]    R. Flouty and G. Estephane. Bioaccumulation and biosorption of copper and lead by a unicellular algae *Chlamydomonas reinhardtii* in single and binary metal systems: A comparative study. Journal of Environmental Management 111, 106-114 (2012).

[66]    A. M. Y. Chong, Y. S. Wong and N. F. Y. Tam. Performance of different microalgal species in removing nickel and zinc from industrial wastewater. Chemosphere 41, 251-257 (2000).

[67]    C. M. Monteiro, P. M. L. Castro and F. X. Malcata. Cadmium removal by two strains of *Desmodesmus pleiomorphus* cells. Water, Air, and Soil Pollution 208, 17-27 (2009).

[68]    C. Aviles, H. Loza-Tavera, N. Terry and R. Moreno-Sanchez. Mercury pretreatment selects an enhanced cadmium-accumulating phenotype in *Euglena gracilis*. Archives of Microbiology 180, 1-10 (2003).

[69]    S. Shanab, A. Essa and E. Shalaby. Bioremoval capacity of three heavy metals by some microalgae species (Egyptian Isolates). Plant Signaling & Behavior 7, 392-399 (2012).

[70] D. G. Mendoza-Cozatl, E. Rangel-Gonzalez and R. Moreno-Sanchez. Simultaneous $Cd^{2+}$, $Zn^{2+}$, and $Pb^{2+}$ uptake and accumulation by photosynthetic *Euglena gracilis*. Archives of Environmental Contamination and Toxicology 51, 521-528 (2006).

[71] X.-H. Cai, C. Brown, J. Adhiya, S. J. Traina and R. T. Sayre. Growth and heavy metal binding properties of transgenic *Chlamydomonas* expressing a foreign metallothionein gene. International Journal of Phytoremediation 1, 53-65 (1999).

[72] J. Miranda, G. Krishnakumar and A. D'Silva. Removal of $Pb^{2+}$ from aqueous system by live *Oscillatoria laete-virens* (Crouan and Crouan) Gomont isolated from industrial effluents. World Journal of Microbiology and Biotechnology 28, 3053-3065 (2012).

[73] K. K. I. U. Arunakumara, X. Zhang and X. Song. Bioaccumulation of $Pb^{2+}$ and its effects on growth, morphology and pigment contents of *Spirulina (Arthrospira) platensis*. Journal of Ocean University of China 7, 397-403 (2008).

[74] N. Akhtar, J. Iqbal and M. Iqbal. Enhancement of lead(II) biosorption by microalgal biomass immobilized onto loofa (*Luffa cylindrica*) sponge. Engineering in Life Sciences 4, 171-178 (2004).

[75] G. W. Garnham, G. A. Codd and G. M. Gadd. Accumulation of cobalt, zinc and manganese by the estuarine green microalga *Chlorella salina* immobilized in alginate microbeads. Environmental Science & Technology 26, 1764-1770 (1992).

[76] R. Huang, G. Huo, S. Song, Y. Li, L. Xia and J.-F. Gaillard. Immobilization of mercury using high-phosphate culture-modified microalgae. Environmental Pollution 254, 112966 (2019).

[77] A. Ibuot, A. P. Dean, O. A. McIntosh and J. K. Pittman. Metal bioremediation by CrMTP4 over-expressing *Chlamydomonas reinhardtii* in comparison to natural wastewater-tolerant microalgae strains. Algal Research 24, 89-96 (2017).

[78] Y. Li, S. Song, L. Xia, H. Yin, J. V. García Meza and W. Ju. Enhanced Pb(II) removal by algal-based biosorbent cultivated in high-phosphorus cultures. Chemical Engineering Journal 361, 167-179 (2019).

[79] S. Wilkinson, K. Goulding and P. Robinson. Mercury removal by immobilized algae in batch culture systems. Journal of Applied Phycology 2, 223-230 (1990).

[80] S. Siripornadulsil, S. Traina, D. P. Verma and R. T. Sayre. Molecular mechanisms of proline-mediated tolerance to toxic heavy metals in transgenic microalgae. Plant Cell 14, 2837-2847 (2002).

[81] U. Markel, K. D. Essani, V. Besirlioglu, J. Schiffels, W. R. Streit and U. Schwaneberg. Advances in ultrahigh-throughput screening for directed enzyme evolution. Chemical Society Reviews 49, 233-262 (2020).

[82] J. D. Winkler and K. C. Kao. Recent advances in the evolutionary engineering of industrial biocatalysts. Genomics 104, 406-411 (2014).

[83] K. K. Yang, Z. Wu and F. H. Arnold. Machine-learning-guided directed evolution for protein engineering. Nature Methods 16, 687-694 (2019).

[84] J. D. Winkler, C. Garcia, M. Olson, E. Callaway and K. C. Kao. Evolved

osmotolerant *Escherichia coli* mutants frequently exhibit defective *N*-acetylglucosamine catabolism and point mutations in cell shape-regulating protein MreB. Applied and Environmental Microbiology 80, 3729-3740 (2014).

[85]   J. Yang, S. W. Seo, S. Jang, S. I. Shin, C. H. Lim, T. Y. Roh and G. Y. Jung. Synthetic RNA devices to expedite the evolution of metabolite-producing microbes. Nature Communications 4, 1413 (2013).

[86]   R. C. Merrifield, C. Stephan and J. R. Lead. Quantification of Au nanoparticle biouptake and distribution to freshwater algae using single cell - ICP-MS. Environmental Science & Technology 52, 2271-2277 (2018).

[87]   H. Wang, B. Chen, M. He and B. Hu. A facile droplet-chip-time-resolved inductively coupled plasma mass spectrometry online system for determination of zinc in single cell. Analytical Chemistry 89, 4931-4938 (2017).

[88]   Y. Han, C. Ding, J. Zhou and Y. Tian. Single probe for imaging and biosensing of pH, $Cu^{2+}$ ions, and $pH/Cu^{2+}$ in live cells with ratiometric fluorescence signals. Analytical Chemistry 87, 5333-5339 (2015).

[89]   S. B. Maity, S. Banerjee, K. Sunwoo, J. S. Kim and P. K. Bharadwaj. A fluorescent chemosensor for $Hg^{2+}$ and $Cd^{2+}$ ions in aqueous medium under physiological pH and its applications in imaging living cells. Inorganic Chemistry 54, 3929-3936 (2015).

[90]   Q. Meng, R. Zhang, H. Jia, X. Gao, C. Wang, Y. Shi, A. V. Everest-Dass and Z. Zhang. A reversible fluorescence chemosensor for sequentially quantitative monitoring copper and sulfide in living cells. Talanta 143, 294-301 (2015).

[91]   E. C. Jensen. Use of fluorescent probes: their effect on cell biology and limitations. The Anatomical Record: Advances in Integrative Anatomy and Evolutionary Biology 295, 2031-2036 (2012).

[92]   A. K. Lau, H. C. Shum, K. K. Wong and K. K. Tsia. Optofluidic time-stretch imaging - an emerging tool for high-throughput imaging flow cytometry. Lab on a Chip 16, 1743-1756 (2016).

[93]   H. Mikami, C. Lei, N. Nitta, T. Sugimura, T. Ito, Y. Ozeki and K. Goda. High-speed imaging meets single-cell analysis. Chemistry 4, 2278-2300 (2018).

[94]   C. Lei, H. Kobayashi, Y. Wu, M. Li, A. Isozaki, A. Yasumoto, H. Mikami, T. Ito, N. Nitta, T. Sugimura, M. Yamada, Y. Yatomi, D. Di Carlo, Y. Ozeki and K. Goda. High-throughput imaging flow cytometry by optofluidic time-stretch microscopy. Nature Protocols 13, 1603-1631 (2018).

[95]   T. Blasi, H. Hennig, H. D. Summers, F. J. Theis, J. Cerveira, J. O. Patterson, D. Davies, A. Filby, A. E. Carpenter and P. Rees. Label-free cell cycle analysis for high-throughput imaging flow cytometry. Nature Communications 7, 10256 (2016).

[96]   H. Kobayashi, C. Lei, Y. Wu, C. J. Huang, A. Yasumoto, M. Jona, W. Li, Y. Wu, Y. Yalikun, Y. Jiang, B. Guo, C. W. Sun, Y. Tanaka, M. Yamada, Y. Yatomi and K. Goda. Intelligent whole-blood imaging flow cytometry for simple, rapid, and cost-effective drug-susceptibility testing of leukemia. Lab on a Chip 19, 2688-2698

(2019).

[97] Y. Zhou, A. Yasumoto, C. Lei, C. J. Huang, H. Kobayashi, Y. Wu, S. Yan, C. W. Sun, Y. Yatomi and K. Goda. Intelligent classification of platelet aggregates by agonist type. eLife 9, e52938 (2020).

[98] C. McCallum, J. Riordon, Y. Wang, T. Kong, J. B. You, S. Sanner, A. Lagunov, T. G. Hannam, K. Jarvi and D. Sinton. Deep learning-based selection of human sperm with high DNA integrity. Communications Biology 2, 250 (2019).

[99] A. Isozaki, H. Mikami, K. Hiramatsu, S. Sakuma, Y. Kasai, T. Iino, T. Yamano, A. Yasumoto, Y. Oguchi, N. Suzuki, Y. Shirasaki, T. Endo, T. Ito, K. Hiraki, M. Yamada, S. Matsusaka, T. Hayakawa, H. Fukuzawa, Y. Yatomi, F. Arai, D. Di Carlo, A. Nakagawa, Y. Hoshino, Y. Hosokawa, S. Uemura, T. Sugimura, Y. Ozeki, N. Nitta and K. Goda. A practical guide to intelligent image-activated cell sorting. Nature Protocols 14, 2370-2415 (2019).

[100] A. Isozaki, H. Mikami, H. Tezuka, H. Matsumura, K. Huang, M. Akamine, K. Hiramatsu, T. Iino, T. Ito, H. Karakawa, Y. Kasai, Y. Li, Y. Nakagawa, S. Ohnuki, T. Ota, Y. Qian, S. Sakuma, T. Sekiya, Y. Y. Shirasaki, N. Suzuki, E. Tayyabi, T. Wakamiya, M. Xu, M. Yamagishi, H. Yan, Q. Yu, S. Yan, D. Yuan, W. Zhang, Y. Zhao, F. Arai, R. E. Campbell, C. Danelon, D. Di Carlo, K. Hiraki, Y. Hoshino, Y. Hosokawa, M. Inaba, A. Nakagawa, Y. Ohya, M. Oikawa, S. Uemura, Y. Ozeki, T. Sugimura, N. Nitta and K. Goda. Intelligent image-activated cell sorting 2.0. Lab on a Chip 20, 2263-2273 (2020).

[101] N. Nitta, T. Sugimura, A. Isozaki, H. Mikami, K. Hiraki, S. I. Sakuma, T. ino, F. Arai, T. Endo, Y. Fujiwaki, H. Fukuzawa, M. Hase, T. Hayakawa, K. Hiramatsu, Y. Hoshino, M. Inaba, T. Ito, H. Karakawa, Y. Kasai, K. Koizumi, S. W. Lee, C. Lei, M. Li, T. Maeno, S. Matsusaka, D. Murakami, A. Nakagawa, Y. Oguchi, M. Oikawa, T. Ota, K. Shiba, H. Shintaku, Y. Shirasaki, K. Suga, Y. Suzuki, N. Suzuki, Y. Tanaka, H. Tezuka, C. Toyokawa, Y. Yalikun, M. Yamada, M. Yamagishi, T. Yamano, A. Yasumoto, Y. Yatomi, M. Yazawa, D. Di Carlo, Y. Hosokawa, S. Uemura, Y. Ozeki and K. Goda. Intelligent image-activated cell sorting. Cell 175, 266-276. (2018).

[102] Y. Gu, A. C. Zhang, Y. Han, J. Li, C. Chen and Y. H. Lo. Machine learning based real-time image-guided cell sorting and classification. Cytometry A 95, 499-509 (2019).

[103] A. A. Nawaz, M. Urbanska, M. Herbig, M. Notzel, M. Krater, P. Rosendahl, C. Herold, N. Toepfner, M. Kubankova, R. Goswami, S. Abuhattum, F. Reichel, P. Muller, A. Taubenberger, S. Girardo, A. Jacobi and J. Guck. Intelligent image-based deformation-assisted cell sorting with molecular specificity. Nature Methods 17, 595-599 (2020).

[104] N. Nitta, T. Iino, A. Isozaki, M. Yamagishi, Y. Kitahama, S. Sakuma, Y. Suzuki, H. Tezuka, M. Oikawa, F. Arai, T. Asai, D. Deng, H. Fukuzawa, M. Hase, T. Hasunuma, T. Hayakawa, K. Hiraki, K. Hiramatsu, Y. Hoshino, M. Inaba, Y. Inoue, T. Ito, M. Kajikawa, H. Karakawa, Y. Kasai, Y. Kato, H. Kobayashi, C. Lei, S.

Matsusaka, H. Mikami, A. Nakagawa, K. Numata, T. Ota, T. Sekiya, K. Shiba, Y. Shirasaki, N. Suzuki, S. Tanaka, S. Ueno, H. Watarai, T. Yamano, M. Yazawa, Y. Yonamine, D. Di Carlo, Y. Hosokawa, S. Uemura, T. Sugimura, Y. Ozeki and K. Goda. Raman image-activated cell sorting. Nature Communications 11, 3452 (2020).

[105] M. Einicker-Lamas, G. Antunes Mezian, T. Benevides Fernandes, F. L. S. Silva, F. Guerra, K. Miranda, M. Attias and M. M. Oliveira. *Euglena gracilis* as a model for the study of $Cu^{2+}$ and $Zn^{2+}$ toxicity and accumulation in eukaryotic cells. Environmental Pollution 120, 779-786 (2002).

[106] M. G. Santiago-Martinez, E. Lira-Silva, R. Encalada, E. Pineda, J. C. Gallardo-Perez, A. Zepeda-Rodriguez, R. Moreno-Sanchez, E. Saavedra and R. Jasso-Chavez. Cadmium removal by *Euglena gracilis* is enhanced under anaerobic growth conditions. Journal of Hazardous Materials 288, 104-112 (2015).

[107] R. Sánchez-Thomas, J. D. García-García, Á. Marín-Hernández, J. P. Pardo, S. Rodríguez-Enríquez, R. Vera-Estrella, A. López-Macay and R. Moreno-Sánchez. The intracellular water volume modulates the accumulation of cadmium in *Euglena gracilis*. Algal Research 46, 101774 (2020).

[108] B. Khatiwada, M. T. Hasan, A. Sun, K. S. Kamath, M. Mirzaei, A. Sunna and H. Nevalainen. Probing the role of the chloroplasts in heavy metal tolerance and accumulation in *Euglena gracilis*. Microorganisms 8, 115 (2020).

[109] J. D. Garcia-Garcia, K. A. Pena-Sanabria, R. Sanchez-Thomas and R. Moreno-Sanchez. Nickel accumulation by the green algae-like *Euglena gracilis*. Journal of Hazardous Materials 343, 10-18 (2018).

[110] J. D. Garcia-Garcia, J. S. Rodriguez-Zavala, R. Jasso-Chavez, D. Mendoza-Cozatl and R. Moreno-Sanchez. Chromium uptake, retention and reduction in photosynthetic *Euglena gracilis*. Archives of Microbiology 191, 431-440 (2009).

[111] S. Tahira, S. Khan, S. Samrana, L. Shahi, I. Ali, W. Murad, Z. u. Rehman and A. Azizullah. Bio-assessment and remediation of arsenic (arsenite As-III) in water by *Euglena gracilis*. Journal of Applied Phycology 31, 423-433 (2018).

[112] A. Pal, J. Jayamani and R. Prasad. An urgent need to reassess the safe levels of copper in the drinking water: Lessons from studies on healthy animals harboring no genetic deficits. NeuroToxicology 44, 58-60 (2014).

[113] Y. Ding, L. Yu, C. Zhang, H. He, B. Zhang, Q. Liu, D. Yu and X. Xing. High-throughput microfluidic particle velocimetry using optical time-stretch microscopy. Applied Physics Letters 115, 033702 (2019).

[114] K. Goda, A. Ayazi, D. R. Gossett, J. Sadasivam, C. K. Lonappan, E. Sollier, A. M. Fard, S. C. Hur, J. Adam, C. Murray, C. Wang, N. Brackbill, D. Di Carlo and B. Jalali. High-throughput single-microparticle imaging flow analyzer. Proceedings of the National Academy of Sciences of the United States of America 109, 11630-11635 (2012).

[115] K. Goda and B. Jalali. Dispersive Fourier transformation for fast continuous single-shot measurements. Nature Photonics 7, 102-112 (2013).

[116] K. Goda, K. K. Tsia and B. Jalali. Serial time-encoded amplified imaging for real-time observation of fast dynamic phenomena. Nature 458, 1145-1149 (2009).

[117] J. L. Wu, Y. Q. Xu, J. J. Xu, X. M. Wei, A. C. Chan, A. H. Tang, A. K. Lau, B. M. Chung, H. Cheung Shum, E. Y. Lam, K. K. Wong and K. K. Tsia. Ultrafast laser-scanning time-stretch imaging at visible wavelengths. Light: Science & Applications 6, e16196 (2017).

[118] C. Lei, B. Guo, Z. Cheng and K. Goda. Optical time-stretch imaging: Principles and applications. Applied Physics Reviews 3, 011102 (2016).

[119] M. Xu, J. Harmon, D. Yuan, S. Yan, C. Lei, K. Hiramatsu, Y. Zhou, M. H. Loo, T. Hasunuma, A. Isozaki and K. Goda. Morphological indicator for directed evolution of *Euglena gracilis* with a high heavy metal removal efficiency. Environmental Science & Technolology 55, 7880-7889 (2021).

[120] R. A. Andersen, J. A. Berges, P. J. Harrison and M. M. Watanabe, Recipes for freshwater and seawater media, in: R. A. Andersen (Ed.) Algal culturing techniques, Elsevier Academic Press, Berlington, 2005, pp. 429−538.

[121] A. E. Carpenter, T. R. Jones, M. R. Lamprecht, C. Clarke, I. H. Kang, O. Friman, D. A. Guertin, J. H. Chang, R. A. Lindquist, J. Moffat, P. Golland and D. M. Sabatini. CellProfiler: image analysis software for identifying and quantifying cell phenotypes. Genome Biology 7, R100 (2006).

[122] L. Kamentsky, T. R. Jones, A. Fraser, M. A. Bray, D. J. Logan, K. L. Madden, V. Ljosa, C. Rueden, K. W. Eliceiri and A. E. Carpenter. Improved structure, function and compatibility for CellProfiler: modular high-throughput image analysis software. Bioinformatics 27, 1179-1180 (2011).

[123] N. Cristianini and J. Shawe-Taylor, An introduction to support vector machines and other kernel-based learning methods, Cambridge University Press, Cambridge, U. K., 2000.

[124] V. Kecman, Support vector machines–an introduction, in: L. Wang (Ed.) Support vector machines: theory and applications, Springer, Berlin, Heidelberg, New York, 2005, pp. 1-47.

[125] I. H Witten, E. Frank, M. A Hall and C. J Pal, Data mining: practical machine learning tools and techniques, Morgan Kaufmann, Cambridge, MA, U. S. A., 2016.

[126] K. Y.-H. Gin, Y.-Z. Tang and M. A. Aziz. Derivation and application of a new model for heavy metal biosorption by algae. Water Research 36, 1313-1323 (2002).

[127] A. Gunther, J. Raff, G. Geipel and G. Bernhard. Spectroscopic investigations of U(VI) species sorbed by the green algae *Chlorella vulgaris*. Biometals 21, 333-341 (2008).

[128] J. Jena, N. Pradhan, R. R. Nayak, B. P. Dash, L. B. Sukla, P. K. Panda and B. K. Mishra. Microalga *Scenedesmus* sp.: A potential low-cost green machine for silver nanoparticle synthesis. Journal of Microbiology and Biotechnology 24, 522-533 (2014).

[129] Y. Collos, F. Mornet, A. Sciandra, N. Waser, A. Larson and P. J. Harrison. An

optical method for the rapid measurement of micromolar concentrations of nitrate in marine phytoplankton cultures. Journal of Applied Phycology 11, 179-184 (1999).

[130] M. Li, H. E. Muñoz, K. Goda and D. Di Carlo. Shape-based separation of microalga *Euglena gracilis* using inertial microfluidics. Scientific Reports 7, 10802 (2017).

[131] M. Masaeli, E. Sollier, H. Amini, W. Mao, K. Camacho, N. Doshi, S. Mitragotri, A. Alexeev and D. Di Carlo. Continuous inertial focusing and separation of particles by shape. Physical Review X 2, 031017 (2012).

[132] H. Z. Hill, J. A. Schiff and H. T. Epstein. Studies of chloroplast development in *Euglena*: XIII. Variation of ultraviolet sensitivity with extent of chloroplast development. Biophysical Journal 6, 125-133 (1966).

[133] K. Yamada, H. Suzuki, T. Takeuchi, Y. Kazama, S. Mitra, T. Abe, K. Goda, K. Suzuki and O. Iwata. Efficient selective breeding of live oil-rich *Euglena gracilis* with fluorescence-activated cell sorting. Scientific Reports 6, 26327 (2016).

[134] B. Liu, Z. Sun, X. Ma, B. Yang, Y. Jiang, D. Wei and F. Chen. Mutation breeding of extracellular polysaccharide-producing microalga *Crypthecodinium cohnii* by a novel mutagenesis with atmospheric and room temperature plasma. International Journal of Molecular Sciences 16, 8201-8212 (2015).

[135] S. Cao, X. Zhou, W. Jin, F. Wang, R. Tu, S. Han, H. Chen, C. Chen, G. J. Xie and F. Ma. Improving of lipid productivity of the oleaginous microalgae *Chlorella pyrenoidosa* via atmospheric and room temperature plasma (ARTP). Bioresource Technology 244, 1400-1406 (2017).